Evidence of Wildfires and Elevated Atmospheric Oxygen at the Frasnian–Famennian Boundary in New York (USA): Implications for the Late Devonian Mass Extinction

Zeyang Liu[1], David Selby[1,4], Paul C. Hackley[2], and D. Jeffrey[3]

[1]*Department of Earth Sciences, University of Durham, Durham DH1 3LE, UK*

[2]*U.S. Geological Survey, MS 956 National Center, Reston, VA 20192, USA*

[3]*Department of Geological Sciences, SUNY College at Geneseo, Geneseo, NY 14454, USA*

[4]*State Key Laboratory of Geological Processes and Mineral Resources, School of Earth Resources, China University of Geosciences, Wuhan, 430074, Hubei, China*

Corresponding author: Zeyang Liu (geozy.liu@outlook.com)

ABSTRACT

The Devonian Period experienced significant fluctuations of atmospheric oxygen (O_2) levels (~25 – 13%), for which the extent and timing are debated. Also characteristic of the Devonian Period, at the Frasnian–Famennian (F–F) boundary, is one of the 'big five' mass extinction events of the Phanerozoic. Fossilized charcoal (inertinite) provides a record of wildfire events, which in turn can provide insight into the evolution of terrestrial ecosystems and the atmospheric composition. Here, we report organic petrology, programmed pyrolysis analysis, major and trace element analyses and initial osmium isotope (Os_i) stratigraphy from five sections of Upper Devonian (F–F interval) from western New York, USA. These data are discussed to infer evidence of a wildfire event at the Frasnian–Famennian boundary. Based on the evidence for a wildfire at the F–F we also provide an estimate of atmospheric O_2 level of ~23 – 25% at this interval, which is in agreement with the models that predict elevated pO_2 levels during the Late Devonian. This, coupled with our Os isotope records, support the currently published Os_i data that lacks any evidence for an extra-terrestrial impact or volcanic event at the F-F interval, and therefore to act as a trigger for the F–F mass extinction. The elevated O_2 level at the F-F inferred from this study supports the hypothesis that pCO_2 drawdown and associated climate cooling may have acted as a driving mechanism of the F–F mass extinction.

INTRODUCTION

During the Devonian Period, the level of atmospheric O_2 is suggested to have significantly fluctuated in response to the diversification and radiation of terrestrial plant life, and to have driven the size increase in fauna (Dahl et al., 2010). Currently debated is the timing and amount of O_2 change throughout the Devonian into the Carboniferous. For example, O_2 levels are estimated to have dropped from ~25 % to ~13 % during the Devonian, with levels rising steadily to present day atmospheric levels (21 %) by the mid-Mississippian Epoch (Berner, 2006; Rimmer et al., 2015; Scott and Glasspool, 2006). In contrast, O_2 levels are also suggested to have dropped from ~25 % during the Early Devonian to ~17 % in the early Late Devonian, and then increased to ~22 % during Late Devonian (Berner et al., 2003; Berner, 2009). In addition to the atmospheric O_2 response related to the evolution of flora and fauna, a positive feedback between atmospheric O_2 and episodes of wildfire has been proposed, whereby higher O_2 concentrations are related to higher frequencies of fire events that result in charcoal production and burial (Berner et al., 2003). This burial of black carbon leads to pCO_2 drawdown that, in turn, creates a further increase in atmospheric O_2 (Berner et al., 2003). Inertinite macerals, the by-product of wildfires, provide a record of wildfire events and inertinite presence in the sedimentary record has been used to infer ancient atmospheric O_2 levels (Scott and Glasspool, 2007; Glasspool and Scott, 2010).

In addition to fluctuations in atmospheric O_2, the Devonian Period also witnessed the Frasnian–Famennian (F–F) mass extinction, which is one of the 'big five' mass extinction events of the Phanerozoic (Stanley, 2016). Proposed extinction mechanisms for this Devonian extinction include ocean anoxic or euxinic conditions (Bond et al., 2004), climate cooling (Huang et al., 2018; Joachimski and Buggisch, 2002; Joachimski et al., 2009), sea-level change (Johnson et al., 1985; Bond and Wignall, 2008), bolide impact (Claeys et al., 1992), and volcanism (Racki et al., 2018).

This paper presents new organic petrology, programmed pyrolysis analysis, major and trace element analyses, and initial osmium isotope ($^{187}Os/^{188}Os_i$, Os_i) stratigraphy, of samples from five Upper Devonian (F–F interval) sections from western New York, USA, and discusses the evidence for wildfire events at the F–F boundary and, by inference, the level of atmospheric O_2 (and implied pCO_2 levels) and the possible mechanisms (e.g., wildfire, volcanism, climate change, etc.) that led to the F–F mass extinction.

GEOLOGICAL BACKGROUND

In western New York State (USA), the sedimentary record of the F–F interval consists of siliciclastic mudstones and sandstones that are interpreted as slope to basin deposits of the northern Appalachian foreland basin (Fig. 1; Sageman et al., 2003; Over, 1997). This study focuses on five measured sections (Fig. 1), four of which are from outcrops (Irish Gulf, IG; Beaver Meadow Creek, BMC; Walnut Creek Bank, WCB; and Joint Creek, JC) and one from a drill core (West Valley, WV). These sections are interpreted as proximal to distal deposits (JC, BMC, WV, IG and WCB, respectively; Fig. 1).

In all sections, the Frasnian–Famennian (F–F) interval is mapped as Late Frasnian and earliest Famennian Hanover Formation and the Early Famennian Dunkirk Formation (Over, 2002). The Hanover Formation comprises light gray, silty shale and interbedded black silty shale that is rich in organic matter (~0.5–5 wt. % TOC), which is of low thermal maturity (%BR_o ~ 0.6, solid bitumen reflectance). The BR_o values are used here as a proxy for thermal maturity which are equivalent to or slightly less than the VR_o at this thermal maturity (Wei et al., 2016; Hackley and Lewan, 2018). The gray shale is intensively bioturbated and contains poorly preserved brachiopods and bivalves. The black shale is pyrite-rich, finely laminated (except the basal parts where bioturbation is observed) and is interpreted as having accumulated in anoxic/dysoxic conditions (Over, 2002). The Hanover Formation is overlain

by the Dunkirk Formation, which contains distinctive beds of black shale. In all sections, the F–F boundary is defined by the first occurrence of the conodont *Palmatolepsis triangularis* (Fig. 2; Klapper et al., 1993; Over, 1997, 2002), and this boundary occurs in a regionally continuous bed of black shale that is correlated with the upper Kellwasser Horizon.

METHODS

Across the F–F boundary interval black shale beds were sampled at 2 – 5 cm stratigraphic resolution. Above and below the F–F boundary the black shale units were sampled at a lower resolution of approximately 5 – 10 cm.

Organic Petrology, Programmed Pyrolysis, and Total Organic Carbon Analysis

Eighty-seven samples were prepared by ASTM D2797 for petrographic analyses at the U.S. Geological Survey (USGS) in Reston, Virginia, using a thermoset plastic briquette mount, which was ground and polished with successively finer abrasives until a 0.05-micrometer (µm) finishing stage. Solid bitumen reflectance analyses (BR_o, %) were collected according to ASTM D7708. Generally, at least 20 measurements of solid bitumen reflectance were collected for each sample, with only 1 measurement per individual rock fragment. Sample briquettes were imaged under oil immersion on a Zeiss AxioImager microscope in white and blue incident light at 500x magnification. A Leica DM4000 microscope equipped with LED illumination and monochrome camera detection was used for solid bitumen reflectance analysis with the computer program DISKUS-FOSSIL by Hilgers Technisches Buero. A YAG calibration standard (0.908% R_o) from Klein and Becker was used. Inertinite reflectance (IR_o, %) was measured with the same method as solid bitumen. Samples were point-counted (300 – 500 points per sample) to determine relative abundances of mineral matter and macerals, which are inertinite, solid bitumen and telalginite (*Tasmanites*) that presented in our sample sets. Bulk geochemical analyses were determined on the powdered

samples after crushing with a shatterbox. Bulk analyses included total organic carbon (TOC) content by LECO carbon analyzer and hydrocarbon analyzer with kinetics (HAWK) programmed pyrolysis (analyzed at the USGS in Denver, Colorado) using methods outlined in Espitalié et al. (1985).

Re–Os Analysis

Rhenium-osmium (Re-Os) analysis was undertaken at the Laboratory for Sulphide and Source Rock Geochronology and Geochemistry of Durham University (UK). Samples were polished to remove any potential weathered surface and drilling marks. All samples were powdered in a Zirconium dish using a shatterbox. Powdered sample (~1 g) and a known amount of spike (mixed ^{185}Re + ^{190}Os) were digested in a Carius tube with 8 ml of 0.25 g/g CrO_3 in 4 N H_2SO_4 at 220 °C for 48 h. Rhenium was isolated using NaOH–acetone extraction and anion chromatography. Osmium was isolated by solvent (chloroform) extraction and purified by micro–distillation. The purified Re and Os fractions were analysed via negative thermal ionization mass spectrometry using a Thermo Finnigan TRITON mass spectrometer in the Arthur Holmes Laboratory at Durham University via static Faraday cup for Re and secondary electron multiplier for Os. Total procedural blanks during this study were 12.5 ± 4.5 pg and 0.12 ± 0.06 pg (1σ S.D., n = 3) for Re and Os, respectively, with an average $^{187}Os/^{188}Os$ value of 0.34 ± 0.20 (n = 3). The initial $^{187}Os/^{188}Os$ values were calculated using the following equation:

$$^{187}Os/^{188}Os_{initial} = {}^{187}Os/^{188}Os_{measured} - (^{187}Re/^{188}Os_{measured} * (EXP(\lambda * t) - 1))$$

where λ is ^{187}Re decay constant $1.666e^{-11}$ a^{-1} (Smoliar et al., 1996), and t is the F–F boundary age (371.93 Ma; Percival et al., 2018).

Major and Trace Element Analysis

Aliquots of the sample powder prepared for Re–Os analysis were also used for major and trace element analysis. Major and trace element abundances were determined using a Panalytical Zetium X–ray fluorescence (XRF) spectrometer at Department of Geography at Durham University. Major and trace elements were analyzed with fused bead and pressed pellet, respectively. For the former, 0.6 g of sample powder and 6 g of flux were used to fuse the bead. The pressed pellet was prepared with 12 g of sample and 3 g of binder. Reproducibility and precision were demonstrated through the repeated analysis of standards (USGS SBC–1, USGS SDO–1). Uncertainty is less than 1 % for major elements (Si, Al and Ti), less than 10 % for trace elements (Mn, Vi and Ni), and 20 % for Mo.

RESULTS

Results of Organic Petrology and Pyrolysis Data

Three types of macerals (inertinite, alginite, and solid bitumen) were identified in the samples (Fig. 3). Pyrolysis data suggests the dominance of marine organic matter in the samples (Fig. 4). Inertinite is observed in all studied sections (Fig. 2). Traces of inertinite are identified in samples from the JC section below and above the F–F boundary, however, none were counted due to the low abundance (lower than 0.2 %, volume percent of whole rock, here and after). In the BMC section that represents the second-most proximal paleo-setting in the Appalachian Basin studied herein, the first occurrence of inertinite is within Upper Frasnian strata (0.6 %) and continued upward, reaching a maximum (2.2 %) just below the F–F boundary, after which the inertinite concentration decreased to 0.2 % above the F–F boundary. For the remaining WV, WCB, IG sections that represent a more basinward depositional environment, the first occurrence of inertinite is within the lowest Famennian strata. Inertinite abundance in the WV, IG, and WCB section is 0.2 to 0.4 %, 0.2 to 1 % and 0.2 to 1.2 %, respectively.

Solid bitumen reflectance ($BR_{o,}$ %) and T_{max} data suggest that the samples record a

low thermal maturity (%BR_o ~ 0.6, T_{max} ~ 445 °C; Table S7 and S8). Inertinite reflectance (IR_o) values range from 1.74 – 3.16 % (Table S3). In hydrogen and oxygen index space (pseudo Van Krevelen plot; Fig. 4), the majority of samples are characterized by Type II-III kerogen.

Results of Major and Trace Element Analyses

Trace element abundances and ratios can be reliable proxies for paleo-redox environment (e.g., Mn, Mo, and V/[V+Ni]). The Mn values of all of the samples range from 210 to 630 ppm with a mean value of 322 ppm. The majority of the samples have Mn values ranging from 200 to 400 ppm (Fig. 5). The Mo/Al ratio (2.53 – 34.09 × 10^{-4}) exceeds the average shale value (0.32 × 10^{-4}; Wedepohl, 1971), suggesting authigenic enrichment. Average V/Al ratio (14.41 × 10^{-4}) and Ni/Al (7.78 × 10^{-4}) ratios are comparable to those of average shale (14.62 × 10^{-4} and 7.65 × 10^{-4} respectively; Wedepohl, 1971). Only a few samples from the F–F interval of BMC and WV sections have Mn values between 400 – 630 ppm, indicating decreased anoxia for the F–F interval relative to the other intervals. The Mo abundance values (4 to 42 ppm, average 18 ppm) represent a non-euxinic to euxinic depositional environment (Fig. 5; Scott and Lyons, 2012). The Mo values for the F–F interval were typically less than 15 ppm, suggesting a non-euxinic environment. The V/(V+Ni) values range from 0.50 to 0.74, indicating dysoxic to anoxic conditions (Fig. 5; Hatch and Leventhal, 1992). The Mo abundance (4 to 42 ppm, average 18 ppm) across the F–F section coupled to the V/(V+Ni) values of 0.50 to 0.74 and intervals of elevated Mn (400 – 630 ppm) are suggestive of decreased anoxia (Fig. 5; Hatch and Leventhal, 1992; Scott and Lyons, 2012).

Results of Re–Os Analysis

The Re and Os (^{192}Os) abundances, and $^{187}Re/^{188}Os$ and $^{187}Os/^{188}Os$ isotopic compositions, range from 0.9 to 32 ppb and 48 to 460 ppt (18 to 145 ppt), and 97.46 to 658 and 0.80 to 4.85, respectively, across all the sections (Table S4). Stratigraphically, no

relationships are observed between trace metal redox proxies, Re and Os abundances, $^{187}Re/^{188}Os$ and initial $^{187}Os/^{188}Os$ ratios, and TOC values (Fig. 5). Further, there is no apparent correlation between Re and Os abundances and TOC values (Fig. 6). Initial $^{187}Os/^{188}Os$ (Os_i) compositions (calculated at 371.93 Ma; *Percival et al.,* 2018) are broadly the same across the F–F boundary (Fig. 7).

Samples with similar TOC possess significant variation in their Re and Os abundances (up to 30 times for Re and 6 times for Os). At the F–F boundary, the ^{192}Os/TOC ratios for each section are generally identical, but the Re/TOC ratios vary greatly. Overall, no linear relationship exists for Re/TOC and ^{192}Os/TOC. The West Valley 777 unit (F–F boundary) exhibits very limited range in its $^{187}Re/^{188}Os$ compositions (Re/Os fractionation, ~20), whereas the other three units above and below the F–F boundary in the West Valley section and other F–F sections exhibit a relatively large range in $^{187}Re/^{188}Os$ values (200–400). In terms of organic matter composition, the 777 unit is dominated by solid bitumen (~90 %) and has the most limited spread in the HI–OI index plot compared with the other sections (Figs. 4 and 8). The other sections have more variable organic matter composition, especially the JC section (the most proximal section), which shows the largest $^{187}Re/^{188}Os$ fractionation. Elevated Re and ^{192}Os abundances are present only in strata that are interpreted as having accumulated in a highly reduced environment, based on the redox proxies of Mn and V(V+Ni) (Fig. 5). However, samples that are interpreted as having accumulated in reduced environments also have low Re and Os abundances (Fig. 5). The $^{187}Re/^{188}Os$ values are variable across one redox environment, with the $^{187}Re/^{188}Os$ values and their variablity being lower with an increase in oxygen in the water column (Fig. 5). The OI values are predominantly below 20 and show no specific relationship with $^{187}Re/^{188}Os$ within or across the studied locations (Fig. 8). There is no correlation between Re and ^{192}Os abundances and Mo concentration (Fig. 5). The overall $^{187}Re/^{188}Os$ values show no clear correlation with the

198 clastic input proxies (Si/Al and Ti/Al). Individually, each F–F section shows a negative
199 correlation between $^{187}Re/^{188}Os$ values and the clastic input proxies. The samples with more
200 clastic input correlate with lower $^{187}Re/^{188}Os$ values in that section (Fig. 9).

201 **DISCUSSION**

202 **Wildfire and Fire Type**

203 Inertinite as a record of wildfire events can provide vital estimates for the level of atmospheric
204 oxygen and thus implications for the evolution of Earth systems (Glasspool and Scott, 2010; Scott and
205 Glasspool, 2006). Although inertinite may originate from processes (e.g., organic matter
206 degradation by bacterial and fungal activity) other than a wildfire (Hunt and Smyth, 1989;
207 Moore et al., 1996; Taylor et al., 1989), it is unlikely that these processes are the sole cause of all
208 the inertinite observed in this study (Scott and Glasspool, 2007; Glasspool and Scott, 2010 and
209 references therein). The stratigraphic occurrence and relative enrichment of inertinite within each
210 section could be controlled by the proximity of the depositional site to a terrigenous source. Inertinite
211 abundances have been shown to increase with increased proximity to the paleoshoreline, probably due
212 to increased water-borne inertinite contribution (Herring, 1985). A fall in sea level would move the
213 paleoshoreline closer to the sample sites and increase the terrestrial input. The proximal sections of this
214 study have increased inertinite abundance relative to the distal sections. As such, this may be caused by
215 increased detrital input and/or wind-borne origin of inertinite. However, no obvious relationship is
216 observed between inertinite abundance and clastic input proxies (e.g., Ti/Al, Si/Al; Fig. 2). Regional
217 climate also can have an important effect on the wildfire events and thus the inertinite record. Paleomap
218 reconstruction suggests that the source area was located at southern mid-latitudes (Fig. 1), which may
219 have been associated with a subtropical climate. Given the limited stratigraphic interval during which
220 inertinite abundance increase is observed, plate tectonic motion to latitudes associated with a dryer
221 climate is unlikely. Further, the F-F interval records a period of climate cooling of ~6 °C (Huang et al.,

2018). Studies of wildfire events since the Last Glaciation Maximum suggest that a cooler climate would lead to less frequent fire events with less charcoal preservation in the geological record (Power et al., 2008; Daniau, 2010). Thus, the climate cooling at the F-F boundary would likely result in a reduction of inertinite abundance rather than an increase. However, the expansion of land plants throughout the Devonian, specifically trees during the Late Devonian as a result of the development of root systems, resulted in a diverse forest community (Scheckler, 2001; Stein et al., 2012). As such, by the Late Devonian, the dominance of tree Archaeopteris, herbaceous ferns (Rhacophyton) and tree lycopsids (Scheckler, 1986) led to the appearance and increased abundance of inertinite potentially as a result of plants expanding to drier environments that would allow wildfire events to occur. The inertinite abundance therefore is interpreted to suggest increased frequency of wildfire events surrounding the paleosource region of the studied sites during the Frasnian–Famennian interval (Glasspool and Scott, 2010).

Wildfires can be divided into the following three groups: 1) ground fire 2) surface fire; and 3) crown fire; with different burning material and different burning temperatures. Inertinite reflectance is related to the burning temperature as shown by experimental analysis (Scott, 2000; Scott and Glasspool, 2005; Scott and Glasspool, 2007). Based on experimental data, the inertinite reflectance values reported here (1.74 – 3.16 %) correlate to burning temperatures between 400 – 500 °C (Scott and Glasspool, 2007). Although it is known that the temperature provided by reflectance data on wildfire charcoals is a minimum fire temperature (McParland et al., 2009; Scott, 2010) and that the use of such data to determine the nature of wildfires is still at an early stage (Belcher and Hudspith, 2016; Belcher et al., 2018; Roos and Scott, 2018), the temperature range of 400 – 500 °C is indicative of a surface fire, suggesting that the fuel type across the F–F boundary interval would have mainly been herbaceous and shrubby plants, which is consistent with paleo-botanical observations during the Late Devonian (Cressler, 2001; Hudspith et al., 2014; Scheckler, 1986).

Implications for the Rise in Atmospheric O_2 Levels during the early Late Devonian

A wildfire event depends on the combination of fuel and O_2 and the heat source. Throughout geological time, lightning is considered to be the most common source of heat for ignition (Scott and Glasspool, 2006). However, the correlation of mercury data (mercury abundance and mercury/TOC ratios) with inertinite abundance within the F–F interval may suggest that volcanism could have acted as a source of ignition (Racki et al., 2018). The expansion of terrestrial vegetation to develop forests in the Middle Devonian gave rise to a potential ready supply of fuel that could be ignited (Kenrick and Crane, 1997; Stein et al., 2012). However, the hitherto absence of evidence of a fossilized charcoal record, specifically during the Late Frasnian to Early Famennian, has resulted in the prediction of low levels of atmospheric O_2 (17 %) during this time interval (Berner et al., 2003; Rimmer et al., 2015; Scott and Glasspool, 2006). In contrast, the presence of abundant inertinite (average 11.9 %, volume percentage on a mineral-free basis; this study), provides evidence for wildfires and may suggest higher atmospheric O_2 levels during the Latest Fransian. The presence of inertinite is proposed to indicate that the atmospheric O_2 level had at least reached the fire window of 15 % (Belcher and McElwain, 2008).

To date, an equation is only available to estimate the pO_2 level based on the inertinite abundance data of coal/peat (Glasspool and Scott, 2010). This approach utilized maceral data for coals and modern-day peats, and used inertinite abundance data to estimate paleo atmospheric O_2 levels. Here we use inertinite data for Devonian marine shales but apply the same equation. Firstly, there would be a difference between the amount of inertinite preserved in-situ in a mire/peat swamp versus the amount of inertinite that would be found in a marine shale. The inertinite that makes it into the marine shales probably did not originate in a peat swamp but would represent fire events across drier environments where charcoal could move into bodies of water following fire events, either by water or wind transport as discussed above. Therefore, it would not be representative of charcoal occurrences in coeval peats. The relative amounts of organics from a terrestrial environment that can make it into a marine setting differ, and therefore the inertinite abundance may be enhanced on a relative basis given that inertinite is

more recalcitrant than vitrinite (woody tissue) or liptinite (spores, pollen, algae) and thus has an increased chance of surviving water or air transportation (Taylor et al., 1989). Further, this terrestrial component would be diluted by marine organic matter, the amount being dependent on paleoproductivity and preservation rates. The sedimentation rates vary from different sections measured. Secondly, the relative amount of inertinite in the shales is a volumetric estimate, thus additions or losses of other components will influence the reported amount of inertinite. Solid bitumen is a secondary maceral that forms during hydrocarbon generation. Therefore, the compositions reported may not reflect the initial kerogen composition for the shale. Nevertheless, it is reasonable to assume that the inertinite abundance is volumetrically close to the original, as the solid bitumen is replacing the bituminite (Hackley and Cardott, 2016).

Given the above, we use the available equation as an approximation to estimate the Devonian pO_2, although there is different enrichment mechanism of inertinite between coal and shale samples (e.g., preservation, post depositional processes, Taylor et al., 1989). The average inertinite volume percentage amount (12%) of this study estimates the pO_2 level for the F–F boundary interval to be 25 % (24–27 %, see supplementary material). The lower value (24 %) is still considerably higher than the estimated pO_2 value of Early Devonian (~18 %), indicating a rapid rise of pO_2 level. The higher value (~27 %) is comparable to those estimated for Early Carboniferous, suggesting the pO_2 might have reached ~27 % much earlier than previously thought. As discussed above, inertinite in a marine environment could also result from organic matter degradation by bacterial and fungal activity (Hunt and Smyth, 1989; Moore et al., 1996; Taylor et al., 1989). However, such processes result in minimal addition to the inertinite budget (Scott and Glasspool, 2007; Diessel, 2010). It is hard to estimate the maximum amount of non-fire origin inertinite, but even if it is considered that only 50% of the inertinite is a product of fossilized charcoal, the conservatively estimated O_2 level would still be elevated (23 %). Although we emphasize that the inertinite data here used are from marine shale

297 samples and that different inertinite enrichment mechanisms exist between coal and shale deposition, we
298 consider that our data provide an approximation for the pO_2 level at the F–F. Even though this pO_2 level
299 might be an overestimate, because not every inertinite may represent fossilized charcoal (Hunt and
300 Smyth, 1989; Moore et al., 1996; Taylor et al., 1989), our estimated pO_2 value is in agreement with the
301 proposed higher estimated pO_2 value (Glasspool and Scott, 2010) (Fig. 10). The fact that our estimation
302 agrees with Glasspool and Scott (2010) highlights a potential wider application of this model to new
303 samples and localities. Interestingly, our estimation is also in agreement with the GEOCARBSULF
304 model (24 – 25 %; Schachat et al., 2018). Additional models yield lower pO_2 estimations (~17 % from
305 GEOCARBSULFOR and ~20 % from COPSE reload; Krause et al., 2018; Lenton et al., 2018).
306 Previously, models with lower pO_2 levels are preferred as a result of lacking an inertinite record for the
307 F-F interval - the 'charcoal gap' (Scott and Glasspool, 2006). Our finding of inertinite thus provides
308 evidence that supports higher pO_2 levels during this interval. Despite the different estimation of pO_2, all
309 models seem to predict a dramatic rise in pO_2 for the Late Devonian, which correlates with increased
310 inertinite stratigraphically above the F–F boundary as reported from this study and previous work (Fig. 2;
311 Rimmer et al., 2015). As such the atmospheric O_2 level may have reached the present level (21 %) by
312 the Latest Frasnian - Early Famennian (Berner et al., 2003; Berner, 2009), rather than during the Early
313 Mississippian as predicted by previous models (Berner, 2006; Berner, 2009).

314 Additionally, during the F–F interval the atmospheric O_2 level may have been affected by
315 enhanced orogeny activity coupled with sea-level fall that caused increased continental weathering and
316 organic carbon burial (Averbuch et al., 2005; Berner et al., 2003; Bond and Wignall, 2008; Johnson et
317 al., 1985). A radiogenic shift of Os isotopes has been detected immediately before the F-F boundary,
318 indicating enhanced weathering of the continents (Percival et al., 2019). The enhanced weathering, in
319 turn, could have driven an increased nutrition flux to the oceans that would have boosted marine
320 productivity, and led to elevated carbon burial and pCO_2 drawdown (Berner et al., 2003; Huang et al.,
321 2018). All these factors together may have resulted in elevation of the atmospheric O_2 level (Berner et

al., 2003; Huang et al., 2018). Interestingly, the timing of higher O_2 levels within the F–F interval correlates with the radiation of vascular plants and evolution of large animals with a higher O_2 demand (Dahl et al., 2010).

Implications for the Frasnian–Famenian Mass Extinction

The F–F mass extinction has been proposed to have been triggered by an impact and (or) volcanism (Claeys and Casier, 1994; Racki et al., 2018). Volcanism interpreted from Hg data (Racki et al., 2018) and associated weathering of mafic material would have resulted in the delivery of unradiogenic osmium to the ocean that would have caused an unradiogenic excursion in the marine osmium isotope record (Peucker-Ehrenbrink and Ravizza, 2000). However, Os-isotope data (Harris et al., 2013; Gordon et al., 2009; Percival et al., 2019; Turgeon et al., 2007; this study) show no evidence of an unradiogenic osmium isotope excursion (Fig. 7). A possible scenario is that the Hg was not injected into the atmosphere directly from volcanic degassing, but derived from the thermal alteration of organic rich layers during magma emplacement (Svensen et al., 2004). Further, as previously stated (Harris et al., 2013; Gordon et al., 2009; Percival et al., 2019; Turgeon et al., 2007) our Os isotope records do not support an impact scenario, as an impact body would also result in an unradiogenic Os excursion of the marine osmium isotope record (Peucker-Ehrenbrink and Ravizza, 2000). Nevertheless, it is not possible to rule out the scenario of a comet impactor with a very limited meteoritic dust budget that left no elemental spike in the geological record (Jansa, 1993). To date, evidence for a wildfire during the F–F interval is supported by organic geochemistry proxy data [coronene, benzo(ghi)perylene and benzo(e)pyrene] from two sections in Belgium that represent deposition in an epicontinental setting on the southern periphery of the Laurussian continent (Fig.1, Kaiho et al., 2013). This wildfire scenario is questioned by possible secondary processes (such as weathering, diagenetic and oxidative processes) causing the maxima of the combustion proxies and the discrepancy between the lack of a charcoal record

and high combustion proxies (Marynowski and Racki, 2015). However, this argument has been considered unlikely as samples with high and low values have the same lithology and are both well preserved (Kaiho, 2015). Therefore, the inertinite data from the New York sections (this study), and potentially the coronene, benzo(ghi)perylene and benzo(e)pyrene data from Belgium (Kaiho et al., 2013) suggest a potential wildfire event across the F–F boundary interval.

Wildfire has been proposed to destroy plant root systems and lead to enhanced weathering, generate soot and aerosol, and affect the carbon cycle and climate, which then are ultimately linked with major anoxia or extinction events (e.g. Baker et al., 2017; Archibald et al., 2018). However, to determine the scale at which the proposed F–F wildfire burned and to what extent it contributed to the F–F biotic crisis requires further research. Nonetheless, our evidence of elevated O_2 level supports the hypothesis of enhanced mountain-building and continent-weathering that, in turn, may have led to increased marine productivity and carbon burial that resulted in the drawdown of pCO_2 (Averbuch et al., 2005; Berner et al., 2003, Percival et al., 2019). In turn, the pCO_2 drawdown and associated climate cooling may have caused the F–F biotic crisis (Averbuch et al., 2005; Berner et al., 2003; Huang et al., 2018).

Further Insights to $^{187}Re/^{188}Os$ Fractionation in Organic-rich Sedimentary Rocks

In addition to the evaluation and implications of O_2 levels throughout the F–F interval, the organic petrology and geochemistry, coupled with the major and trace element abundances, provide further insight to the fractionation of Re and Os in organic-rich sedimentary rocks. Our data suggest that Re and Os fractionation has no relationship with a redox/euxinc environment (Figs. 5 and 6) and thus excludes deposition under reduced oxygen conditions as the principal controlling factor of Re and Os fractionation (Selby et al., 2009; Harris et al., 2013). The correlation of $^{187}Re/^{188}Os$ ratios with the terrestrial input proxies

(Si/Al and Ti/Al) in each section suggests that a more variable depositional environment is likely to yield more variable Re and Os fractionation (Fig. 9). Samples with homogeneous organic matter composition have relatively limited Re and Os fractionation (Figs. 4 and 9). In contrast, the other samples sets that have more variable organic matter composition have larger Re and Os fractionations (Figs. 4 and 9). This suggest that the organic matter composition/type and its variability may be the mechanism that controls Re and Os fractionation. These findings concur with the findings that a variable depositional environment together with heteorgenous organic matter composition may control Re and Os fractionation (Cumming et al., 2012; Harris et al., 2013).

CONCLUSIONS

The presence of inertinite in Upper Devonian strata within the F–F boundary interval suggests a wildfire event occurred in western New York at this time. The inertinite data also suggest a possibly high atmospheric O_2 level (~ 23 %). Additionally, the Os isotope records do not provide any evidence of an extraterrestrial impact event or volcanic activity as a trigger for the F–F mass extinction. However, the extent of the wildfire event and its possible link with the F–F mass extinction requires further research. Our estimated high O_2 level supports the hypothesis that pCO_2 drawdown and associated climate cooling may have played an important role in the F–F biotic crisis.

ACKNOWLEDGEMENTS

ZL thanks Sandra Clark and David Bausman for hosting him in Reston. We also thank Jin Si Over for field assistance, Brian Slater at the New York State Museum for core samples, Brett Valentine and Javin Hatcherian (USGS-Reston) for laboratory support with organic petrology, Mark Dreier and Augusta Warden (USGS-Lakewood) for TOC and HAWK analysis, and Antonia Hoffman, Chris Ottley and Geoff Nowell for support with Re-

Os analysis. We gratefully acknowledge the TOTAL Endowment Fund and the CUG Wuhan Dida Scholarship to DS, and the University of Durham and China Scholarship Council to ZL. PCH thanks Brett Valentine and Christopher Swezey (USGS-Reston) for reviews of an early version of this manuscript. We also acknowledge the detailed review of the manuscript provided by Chris Reinhard and one anonymous reviewer. A portion of this research was funded by the USGS Energy Resources Program. All data associated with this research are in figures and tables included herein. Any use of trade, firm, or product names is for descriptive purposes only and does not imply endorsement by the U.S. Government.

REFERENCES CITED

Archibald, S., Lehmann, C. E. R., Belcher, C. M., Bond, W. J., Bradstock, R. A., Daniau, A. L., Dexter, K. G., Forrestel, E. J., Greve, M., He, T., Higgins, S. I., Hoffmann, W. A., Lamont, B. B., McGlinn, D. J., Moncrieff, G. R., Osborne, C. P., Pausas, J. G., Price, O., Ripley, B. S., Rogers, B. M., Schwilk, D. W., Simon, M. F., Turetsky, M. R., Van der Werf, G. R., and Zanne, A. E., 2018, Biological and geophysical feedbacks with fire in the Earth system: Environmental Research Letters, v. 13, no. 3, p. 033003.

Averbuch, O., Tribovillard, N., Devleeschouwer, X., Riquier, L., Mistiaen, B., and van Vliet-Lanoe, B., 2005, Mountain building-enhanced continental weathering and organic carbon burial as major causes for climatic cooling at the Frasnian-Famennian boundary (c. 376 Ma)?: Terra Nova, v. 17, no. 1, p. 25-34.

Baker, S. J., Hesselbo, S. P., Lenton, T. M., Duarte, L. V., and Belcher, C. M., 2017, Charcoal evidence that rising atmospheric oxygen terminated Early Jurassic ocean anoxia: Nature Communications, v. 8, p. 15018.

Belcher, C. M., and Hudspith, V. A., 2016, The formation of charcoal reflectance and its potential use in post-fire assessments: International Journal of Wildland Fire, v. 25, no. 7, p. 775-779.

420 Belcher, C. M., and McElwain, J. C., 2008, Limits for Combustion in Low O₂
421 Redefine Paleoatmospheric Predictions for the Mesozoic, v. 321, no. 5893, p. 1197-
422 1200.
423 Belcher, C. M., New, S. L., Santín, C., Doerr, S. H., Dewhirst, R. A., Grosvenor, M. J., and
424 Hudspith, V. A., 2018, What Can Charcoal Reflectance Tell Us About Energy
425 Release in Wildfires and the Properties of Pyrogenic Carbon?: Frontiers in Earth
426 Science, v. 6, no. 169.
427 Berner, R. A., 2006, GEOCARBSULF: A combined model for Phanerozoic atmospheric O2
428 and CO2: Geochimica et Cosmochimica Acta, v. 70, no. 23, p. 5653-5664.
429 Berner, R. A., 2009, Phanerozoic atmospheric oxygen: New results using the
430 GEOCARBSULF model: American Journal of Science, v. 309, no. 7, p. 603-606.
431 Berner, R. A., Beerling, D. J., Dudley, R., Robinson, J. M., and Wildman, R. A., 2003,
432 Phanerozoic atmospheric oxygen: Annual Review of Earth and Planetary Sciences, v.
433 31, no. 1, p. 105-134.
434 Bond, D., Wignall, P. B., and Racki, G., 2004, Extent and duration of marine anoxia during
435 the Frasnian–Famennian (Late Devonian) mass extinction in Poland, Germany,
436 Austria and France: Geological Magazine, v. 141, no. 2, p. 173-193.
437 Bond, D. P. G., and Wignall, P. B., 2008, The role of sea-level change and marine anoxia in
438 the Frasnian–Famennian (Late Devonian) mass extinction: Palaeogeography,
439 Palaeoclimatology, Palaeoecology, v. 263, no. 3–4, p. 107-118.
440 Claeys, P., Casier, J.-G., and Margolis, S. V., 1992, Microtektites and Mass Extinctions:
441 Evidence for a Late Devonian Asteroid Impact: Science, v. 257, no. 5073, p. 1102-
442 1104.

443 Claeys, P., and Casier, J. G., 1994, Microtektite-like impact glass associated with the
444 Frasnian-Famennian boundary mass extinction: Earth and Planetary Science Letters, v.
445 122, no. 3, p. 303-315.
446 Cressler, W. L., 2001, Evidence of earliest known wildfires: Palaios, v. 16, no. 2, p. 171-174.
447 Cumming, V. M., Selby, D., and Lillis, P. G., 2012, Re–Os geochronology of the lacustrine
448 Green River Formation: Insights into direct depositional dating of lacustrine
449 successions, Re–Os systematics and paleocontinental weathering: Earth and Planetary
450 Science Letters, v. 359, p. 194-205.
451 Dahl, T. W., Hammarlund, E. U., Anbar, A. D., Bond, D. P. G., Gill, B. C., Gordon, G. W.,
452 Knoll, A. H., Nielsen, A. T., Schovsbo, N. H., and Canfield, D. E., 2010, Devonian
453 rise in atmospheric oxygen correlated to the radiations of terrestrial plants and large
454 predatory fish: Proceedings of the National Academy of Sciences, v. 107, no. 42, p.
455 17911-17915.
456 Daniau, A-L., 2010, Global patterns of biomass burning during the last glacial period:
457 PAGES News, v. 18, no. 2, p. 61–63.
458 Diessel, C. F. K., 2010, The stratigraphic distribution of inertinite: International Journal of
459 Coal Geology, v. 81, no. 4, p. 251-268.
460 Espitalié, J., Deroo, G., and Marquis, F. J. R. d. l. I. f. d. P., 1985, La pyrolyse Rock-Eval et
461 ses applications. Deuxième partie, v. 40, no. 6, p. 755-784.
462 Glasspool, I. J., and Scott, A. C., 2010, Phanerozoic concentrations of atmospheric oxygen
463 reconstructed from sedimentary charcoal: Nature Geoscience, v. 3, p. 627.
464 Gordon, G. W., Rockman, M., Turekian, K. K., and Over, J., 2009, Osmium isotopic
465 evidence against an impact at the Frasnian-Famennian boundary, v. 309, no. 5, p. 420-
466 430.

467 Hackley, P.C., and Cardott, B.J., 2016, Application of organic petrography in North
468 American shale petroleum systems: a review: International Journal of Coal Geology,
469 v. 163, p. 8-51.
470 Hackley, P. C., and Lewan, M., 2018, Understanding and distinguishing reflectance
471 measurements of solid bitumen and vitrinite using hydrous pyrolysis: Implications to
472 petroleum assessment: AAPG Bulletin, v. 102, no. 6, p. 1119-1140.
473 Harris, N. B., Mnich, C. A., Selby, D., and Korn, D., 2013, Minor and trace element and Re–
474 Os chemistry of the Upper Devonian Woodford Shale, Permian Basin, west Texas:
475 Insights into metal abundance and basin processes: Chemical Geology, v. 356, p. 76-
476 93.
477 Hatch, J. R., and Leventhal, J. S., 1992, Relationship between inferred redox potential of the
478 depositional environment and geochemistry of the Upper Pennsylvanian (Missourian)
479 Stark Shale Member of the Dennis Limestone, Wabaunsee County, Kansas, U.S.A:
480 Chemical Geology, v. 99, no. 1, p. 65-82.
481 Herring, J. R., 1985, Charcoal fluxes into sediments of the north Pacific Ocean: The
482 Cenozoic record of burning, in Sundquist, E. T., and Broecker, W. S., editors, The
483 carbon cycle and atmospheric CO_2: Natural variations Archean to present:
484 Washington D.C., American Geophysical Union, Geophysical Monograph 32, p. 419-
485 442.
486 Huang, C., Joachimski, M. M., and Gong, Y., 2018, Did climate changes trigger the Late
487 Devonian Kellwasser Crisis? Evidence from a high-resolution conodont $\delta^{18}O_{PO4}$
488 record from South China: Earth and Planetary Science Letters, v. 495, p. 174-184.
489 Hudspith, V. A., Belcher, C. M., and Yearsley, J. M., 2014, Charring temperatures are driven
490 by the fuel types burned in a peatland wildfire: Frontiers in Plant Science, v. 5, no.
491 714.

492 Hunt, J. W., and Smyth, M., 1989, Origin of inertinite-rich coals of Australian cratonic basins:
493 International Journal of Coal Geology, v. 11, no. 1, p. 23-46.
494 Jansa, L. F., 1993, Cometary impacts into ocean: their recognition and the threshold
495 constraint for biological extinctions: Palaeogeography, Palaeoclimatology,
496 Palaeoecology, v. 104, no. 1, p. 271-286.
497 Joachimski, M. M., Breisig, S., Buggisch, W., Talent, J. A., Mawson, R., Gereke, M.,
498 Morrow, J. R., Day, J., and Weddige, K., 2009, Devonian climate and reef evolution:
499 Insights from oxygen isotopes in apatite: Earth and Planetary Science Letters, v. 284,
500 no. 3, p. 599-609.
501 Joachimski, M. M., and Buggisch, W., 2002, Conodont apatite $\delta^{18}O$ signatures indicate
502 climatic cooling as a trigger of the Late Devonian mass extinction: Geology, v. 30, no.
503 8, p. 711-714.
504 Johnson, J. G., Klapper, G., and Sandberg, C. A., 1985, Devonian Eustatic Fluctuations in
505 Euramerica: Geological Society of America Bulletin, v. 96, no. 5, p. 567-587.
506 Kaiho, K., 2015, Reply to the comment on Kaiho et al., "A forest fire and soil erosion event
507 during the Late Devonian mass extinction" [Palaeogeogr. Palaeoclimatol. Palaeoecol.
508 392 (2013): 272–280]: Palaeogeography, Palaeoclimatology, Palaeoecology, v. 417, p.
509 573-575.
510 Kaiho, K., Yatsu, S., Oba, M., Gorjan, P., Casier, J.-G., and Ikeda, M., 2013, A forest fire and
511 soil erosion event during the Late Devonian mass extinction: Palaeogeography,
512 Palaeoclimatology, Palaeoecology, v. 392, p. 272-280.
513 Kenrick, P., and Crane, P. R., 1997, The origin and early evolution of plants on land: Nature,
514 v. 389, p. 33.
515 Klapper, G., Feist, R., Becker, R. T., and House, M. R., 1993, Definition of the Frasnian
516 Famennian Stage Boundary: Episodes, v. 16, no. 4, p. 433-441.

Krause, A. J., Mills, B. J. W., Zhang, S., Planavsky, N. J., Lenton, T. M., and Poulton, S. W., 2018, Stepwise oxygenation of the Paleozoic atmosphere: Nature Communications, v. 9, no. 1, p. 4081.

Lenton, T. M., Daines, S. J., and Mills, B. J. W., 2018, COPSE reloaded: An improved model of biogeochemical cycling over Phanerozoic time: Earth-Science Reviews, v. 178, p. 1-28.

Marynowski, L., and Racki, G., 2015, Comment on the Kaiho et al., paper "A forest fire and soil erosion event during the Late Devonian mass extinction" [Palaeogeography, Palaeoclimatology, Palaeoecology 392 (2013): 272–280]: Palaeogeography, Palaeoclimatology, Palaeoecology, v. 417, p. 569-572.

McParland, L. C., Collinson, M. E., Scott, A. C., Campbell, G. J. A., and Sciences, A., 2009, The use of reflectance values for the interpretation of natural and anthropogenic charcoal assemblages, v. 1, no. 4, p. 249.

Moore, T. A., Shearer, J. C., and Miller, S. L., 1996, Fungal origin of oxidised plant material in the Palangkaraya peat deposit, Kalimantan Tengah, Indonesia: Implications for 'inertinite' formation in coal: International Journal of Coal Geology, v. 30, no. 1, p. 1-23.

Over, D. J., 1997, Conodont biostratigraphy of the Java Formation (Upper Devonian) and the Frasnian-Famennian boundary in western New York State, *in* Klapper, G., Murphy, M. A., and Talent, J. A., eds., Paleozoic Sequence Stratigraphy, Biostratigraphy, and Biogeography: Studies in Honor of J. Granville ("Jess") Johnson, Volume 321, Geological Society of America, p. 161-177.

Over, D. J., 2002, The Frasnian/Famennian boundary in central and eastern United States: Palaeogeography, Palaeoclimatology, Palaeoecology, v. 181, no. 1–3, p. 153-169.

Percival, L. M. E., Davies, J. H. F. L., Schaltegger, U., De Vleeschouwer, D., Da Silva, A. C., and Föllmi, K. B., 2018, Precisely dating the Frasnian–Famennian boundary: implications for the cause of the Late Devonian mass extinction: Scientific Reports, v. 8, no. 1, p. 9578.

Percival, L. M. E., Selby, D., Bond, D. P. G., Rakociński, M., Racki, G., Marynowski, L., Adatte, T., Spangenberg, J. E., and Föllmi, K. B., 2019, Pulses of enhanced continental weathering associated with multiple Late Devonian climate perturbations: Evidence from osmium-isotope compositions: Palaeogeography, Palaeoclimatology, Palaeoecology.

Peucker-Ehrenbrink, B., and Ravizza, G., 2000, The marine osmium isotope record: Terra Nova, v. 12, no. 5, p. 205-219.

Power, M. J., Marlon, J., Ortiz, N., Bartlein, P. J., Harrison, S. P., Mayle, F. E., Ballouche, A., Bradshaw, R. H. W., Carcaillet, C., Cordova, C., Mooney, S., Moreno, P. I., Prentice, I. C., Thonicke, K., Tinner, W., Whitlock, C., Zhang, Y., Zhao, Y., Ali, A. A., Anderson, R. S., Beer, R., Behling, H., Briles, C., Brown, K. J., Brunelle, A., Bush, M., Camill, P., Chu, G. Q., Clark, J., Colombaroli, D., Connor, S., Daniau, A.-L., Daniels, M., Dodson, J., Doughty, E., Edwards, M. E., Finsinger, W., Foster, D., Frechette, J., Gaillard, M.-J., Gavin, D. G., Gobet, E., Haberle, S., Hallett, D. J., Higuera, P., Hope, G., Horn, S., Inoue, J., Kaltenrieder, P., Kennedy, L., Kong, Z. C., Larsen, C., Long, C. J., Lynch, J., Lynch, E. A., McGlone, M., Meeks, S., Mensing, S., Meyer, G., Minckley, T., Mohr, J., Nelson, D. M., New, J., Newnham, R., Noti, R., Oswald, W., Pierce, J., Richard, P. J. H., Rowe, C., Sanchez Gon˜i, M. F., Shuman, B. N., Takahara, H., Toney, J., Turney, C., Urrego-Sanchez, D. H., Umbanhowar, C., Vandergoes, M., Vanniere, B., Vescovi, E., Walsh, M., Wang, X., Williams, N., Wilmshurst, J., and Zhang, J. H., 2008, Changes in fire regimes since the Last Glacial

566 Maximum: an assessment based on a global synthesis and analysis of charcoal data:
567 Climate Dynamics, v. 30, no. 7-8, p. 887-907.
568 Racki, G., Rakociński, M., Marynowski, L., and Wignall, P. B., 2018, Mercury enrichments
569 and the Frasnian-Famennian biotic crisis: A volcanic trigger proved?: Geology, v. 46,
570 no. 6, p. 543-546.
571 Rimmer, S. M., Hawkins, S. J., Scott, A. C., and Cressler, W. L., 2015, The rise of fire: Fossil
572 charcoal in late Devonian marine shales as an indicator of expanding terrestrial
573 ecosystems, fire, and atmospheric change: American Journal of Science, v. 315, no. 8,
574 p. 713-733.
575 Roos, C. I., and Scott, A. C., 2018, A comparison of charcoal reflectance between crown and
576 surface fire contexts in dry south-west USA forests %J International Journal of
577 Wildland Fire, v. 27, no. 6, p. 396-406.
578 Sageman, B. B., Murphy, A. E., Werne, J. P., Ver Straeten, C. A., Hollander, D. J., and
579 Lyons, T. W., 2003, A tale of shales: the relative roles of production, decomposition,
580 and dilution in the accumulation of organic-rich strata, Middle–Upper Devonian,
581 Appalachian basin: Chemical Geology, v. 195, no. 1–4, p. 229-273.
582 Schachat, S. R., Labandeira, C. C., Saltzman, M. R., Cramer, B. D., Payne, J. L., and Boyce,
583 C. K., 2018, Phanerozoic pO_2 and the early evolution of terrestrial animals: Proc. R.
584 Soc. B, v. 285, no. 1871, p. 20172631.
585 Scheckler, S. E., 1986, Geology, floristics and paleoecology of Late Devonian coal swamps
586 from Appalachian Laurentia (U.S.A.): Annales de la Société géologique de Belgique,
587 v. 109, p. 209-222.
588 Scheckler, S. E., 2001, Afforestation-the First Forests. In Palaeobiology II (eds D. E. Briggs
589 and P. R. Crowther), p. 67-71.

590 Scott, A. C., 2000, The Pre-Quaternary history of fire: Palaeogeography, Palaeoclimatology,
591 Palaeoecology, v. 164, no. 1, p. 281-329.
592 Scott, A. C., 2010, Charcoal recognition, taphonomy and uses in palaeoenvironmental
593 analysis: Palaeogeography, Palaeoclimatology, Palaeoecology, v. 291, no. 1, p. 11-39.
594 Scott, A. C., and Glasspool, I. J., 2005, Charcoal reflectance as a proxy for the emplacement
595 temperature of pyroclastic flow deposits: Geology, v. 33, no. 7, p. 589-592.
596 Scott, A. C., and Glasspool, I. J., 2006, The diversification of Paleozoic fire systems and
597 fluctuations in atmospheric oxygen concentration: Proceedings of the National
598 Academy of Sciences, v. 103, no. 29, p. 10861-10865.
599 Scott, A. C., and Glasspool, I. J., 2007, Observations and experiments on the origin and
600 formation of inertinite group macerals: International Journal of Coal Geology, v. 70,
601 no. 1, p. 53-66.
602 Scott, C., and Lyons, T. W., 2012, Contrasting molybdenum cycling and isotopic properties
603 in euxinic versus non-euxinic sediments and sedimentary rocks: Refining the
604 paleoproxies: Chemical Geology, v. 324, no. Supplement C, p. 19-27.
605 Selby, D., Mutterlose, J., and Condon, D. J., 2009, U–Pb and Re–Os geochronology of the
606 Aptian/Albian and Cenomanian/Turonian stage boundaries: Implications for timescale
607 calibration, osmium isotope seawater composition and Re–Os systematics in organic-
608 rich sediments: Chemical Geology, v. 265, no. 3, p. 394-409.
609 Smoliar, M. I., Walker, R. J., and Morgan, J. W., 1996, Re-Os ages of group IIA, IIIA, IVA,
610 and IVB iron meteorites: Science, v. 271, no. 5252, p. 1099.
611 Stanley, S. M., 2016, Estimates of the magnitudes of major marine mass extinctions in earth
612 history: Proc Natl Acad Sci U S A, v. 113, no. 42, p. E6325-E6334.

613 Stein, W. E., Berry, C. M., Hernick, L. V., and Mannolini, F., 2012, Surprisingly complex
614 community discovered in the mid-Devonian fossil forest at Gilboa: Nature, v. 483, p.
615 78.
616 Svensen, H., Planke, S., Malthe-Sørenssen, A., Jamtveit, B., Myklebust, R., Rasmussen
617 Eidem, T., and Rey, S. S., 2004, Release of methane from a volcanic basin as a
618 mechanism for initial Eocene global warming: Nature, v. 429, p. 542.
619 Taylor, G. H., Liu, S. Y., and Diessel, C. F. K., 1989, The cold-climate origin of inertinite-
620 rich Gondwana coals: International Journal of Coal Geology, v. 11, no. 1, p. 1-22.
621 Turgeon, S. C., Creaser, R. A., and Algeo, T. J., 2007, Re–Os depositional ages and seawater
622 Os estimates for the Frasnian–Famennian boundary: Implications for weathering rates,
623 land plant evolution, and extinction mechanisms: Earth and Planetary Science Letters,
624 v. 261, no. 3–4, p. 649-661.
625 Wedepohl, K. H., 1971, Environmental influences on the chemical composition of shales and
626 clays: Physics and Chemistry of the Earth, v. 8, no. Supplement C, p. 307-333.
627 Wei, L., Wang, Y., and Mastalerz, M., 2016, Comparative optical properties of macerals and
628 statistical evaluation of mis-identification of vitrinite and solid bitumen from early
629 mature Middle Devonian – Lower Mississippian New Albany Shale: Implications for
630 thermal maturity assessment: International Journal of Coal Geology, v. 168, p. 222-
631 236.

632 FIGURE CAPTIONS

633 Figure 1. Inset map showing present day sample locations – 1: Walnut Creek Bank, 2: Irish
634 Gulf, 3: West Valley, 4: Beaver Meadow Creek, 5: Joint Creek. Paleogeography map after
635 Joachimski et al. (2009) showing location of the Appalachian Basin in North America, and
636 the Belgium Frasnian–Famennian (F–F) sections where organic geochemistry is used to infer
637 a wildfire event at F–F boundary (black square; Kaiho et al., 2013).

638 Figure 2. Inertinite abundance (black circles) and clastic input proxies (Si/Al, open square; Ti/Al, open
639 diamonds). Inertinite abundance is calculated as volume percent of whole rock basis. H: Hanover
640 Formation, D: Dunkirk Formation; Stratigraphic sections are presented in order of proximity to the
641 paleoshoreline = JC: Joint Creek, BMC: Beaver Meadow Creek, WCB: Walnut Creek Bank, IG: Irish
642 Gulf, WV: West Valley; from proximal to distal: JC, BMC, WV, IG, WCB. Gray bars in the Joint
643 Creek section represent samples that contain inertinite, but the inertinite abundance is too low to be
644 counted. The upper top axes are for inertinite bundance. The lower top axes are for Si/Al. The
645 bottom axes are for Ti/Al.

646 Figure 3. Microscopic petrography of macerals through oil immersion. All images, except B
647 and D, are under white light. Images B and D are under blue light. T: telalginite, S: Solid
648 Bitumen, I: Inertinite.

649 Figure 4. Pseudo-Van Krevelen plot (hydrogen index vs. oxygen index) showing kerogen
650 types. Note that for the majority of the samples, the dominant organic matter is solid bitumen,
651 which is a secondary product (not a kerogen) residual from thermal conversion of oil-prone
652 sedimentary organic matter.

653 Figure 5. Stratigraphical plots of TOC, Re, ^{192}Os, $^{187}Re/^{188}Os$, Mo, Mn, and V/(V+Ni). Red
654 line indicates the F–F boundary. No relationships are observed between trace metal redox proxies,
655 Re and ^{192}Os abundances, $^{187}Re/^{188}Os$, and TOC values.

656 Figure 6. Plots of Re, ^{192}Os and $^{187}Re/^{188}Os$ versus Mn, Mo, and V/(V+Ni) for the JC: Joint
657 Creek, BMC: Beaver Meadow Creek, WCB: Walnut Creek Bank, IG: Irish Gulf, and WV: West
658 Valley sections.

659 Figure 7. Initial $^{187}Os/^{188}Os$ isotope stratigraphy for the Frasnian–Famennian interval in New
660 York. Sections are presented in order of proximity to the paleoshoreline = JC: Joint Creek, BMC:
661 Beaver Meadow Creek, WCB: Walnut Creek Bank, IG: Irish Gulf, WV: West Valley; from proximal to

662 distal: JC, BMC, WV, IG, WCB. Biostratigraphy constraints are from Klapper et al. (1993) and
663 Over (1997, 2002). Initial $^{187}Os/^{188}Os$ isotope values calculated at 371.93 Ma (Percival et al.,
664 2018). Uncertainties of the initial $^{187}Os/^{188}Os$ isotope values were determined by error
665 propagation of uncertainties in Re and Os mass spectrometer measurements, blank
666 abundances and isotopic compositions, spike calibrations and reproducibility of standard Re
667 and Os isotopic values. Typically, the range of uncertainty (2σ) of the initial $^{187}Os/^{188}Os$ is
668 smaller than the symbol size.

669 Figure 8. Plots of total organic carbon (TOC) versus Re (A) and ^{192}Os (B), and plots of
670 oxygen index (OI) versus Re (C), ^{192}Os (D), and $^{187}Re/^{188}Os$ (E) for the JC: Joint Creek, BMC:
671 Beaver Meadow Creek, WCB: Walnut Creek Bank, IG: Irish Gulf, and WV: West Valley sections.

672 Figure 9. Summary of results from organic matter (OM) analysis, Re/TOC ratios, and clastic
673 input proxies (Ti/Al and Si/Al). OM color represents organic matter types. Green: telalginite,
674 black: Solid bitumen, gray: Inertinite. Red bar represents the Frasnian–Famennian boundary.
675 Lines represent the broad trend of the data points.

676 Figure 10. Modelled pO_2 level from inertinite abundance modified after Glasspool and Scott (2010). See
677 text for discussion. Line; best estimate on the basis of late Palaeozoic pO_2 maxima of 30%. Ranges of
678 uncertainty ("error bars") are 1 standard deviation (s.d.) from mean. Shaded area; estimate of maximum
679 uncertainty ("error") assuming Phanerozoic pO_2 maxima of 35 % + 1 s.d. (upper margin) and 25 % - 1
680 s.d. (lower margin).

681 [1]GSA Data Repository item 201Xxxx, [[one supplementary text and one data set]], is
682 available online at www.geosociety.org/pubs/ft20XX.htm, or on request from
683 editing@geosociety.org.


~372 Ma
Canada
Buffalo
Batavia
N
Avon
Geneseo
Warsaw
Lake Erie
2
4
Dansville
Silver Creek
Yorkshire
5
Dunkirk
1
Gowanda
3
New York State
0
20 km
SIBERIA
BALTICA
NORTH
AMERICA
PALEOTETHYS
SOUTH
CHINA
NORTH
CHINA
BELGIUM
AFRICA
EAST ANTARCTICA
SOUTH
AMERICA

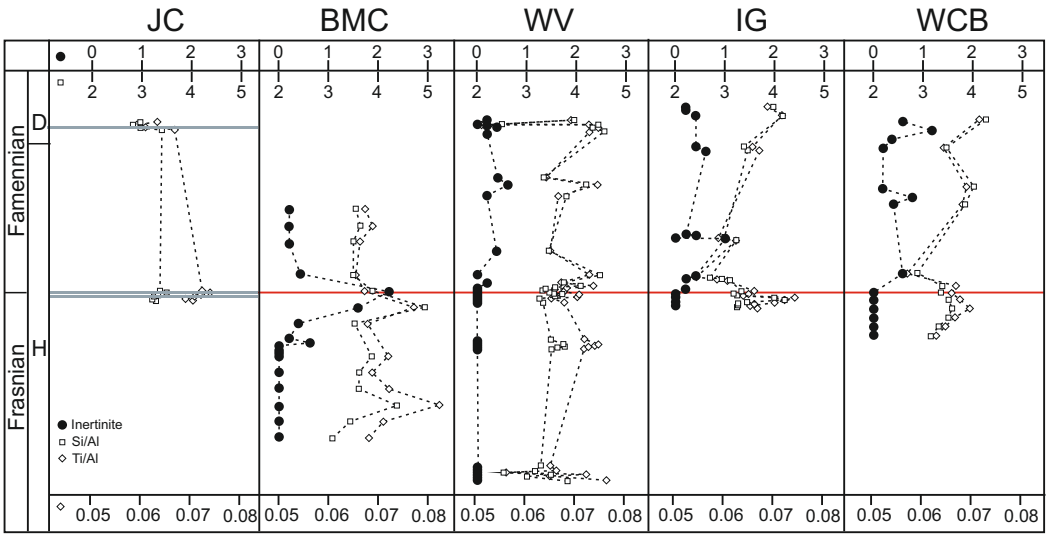
JC
BMC
WV
IG
WCB
Famennian
Frasnian
D
H
Inertinite
Si/Al
Ti/Al
0
1
2
3
2
3
4
5
0.05
0.06
0.07
0.08

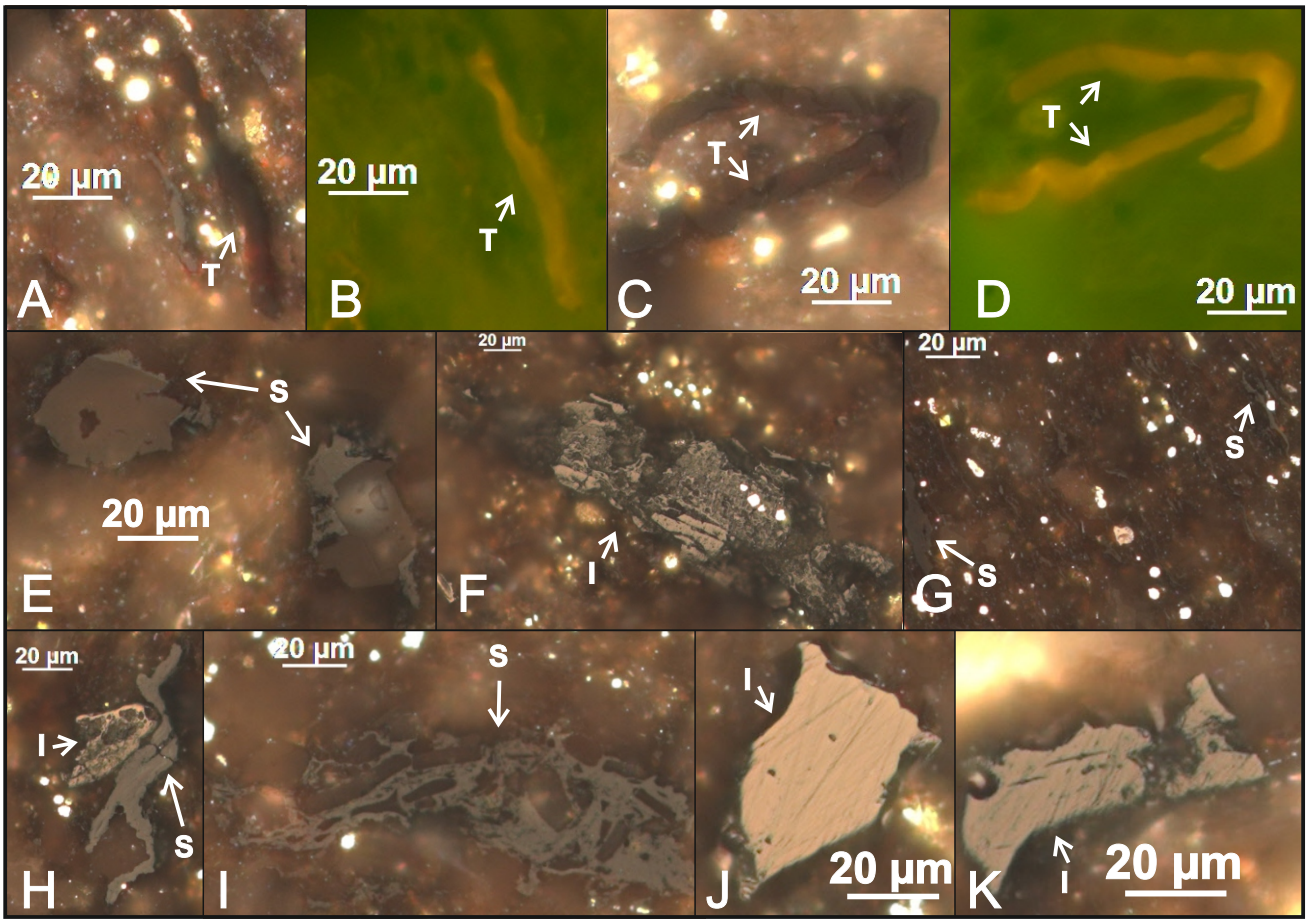
20 µm
T
A
20 µm
T
B
T
C
20 µm
T
D
20 µm
S
20 µm
E
20 µm
I
F
20 µm
S
S
G
20 µm
I
S
H
20 µm
S
I
I
20 µm
J
I
20 µm
K

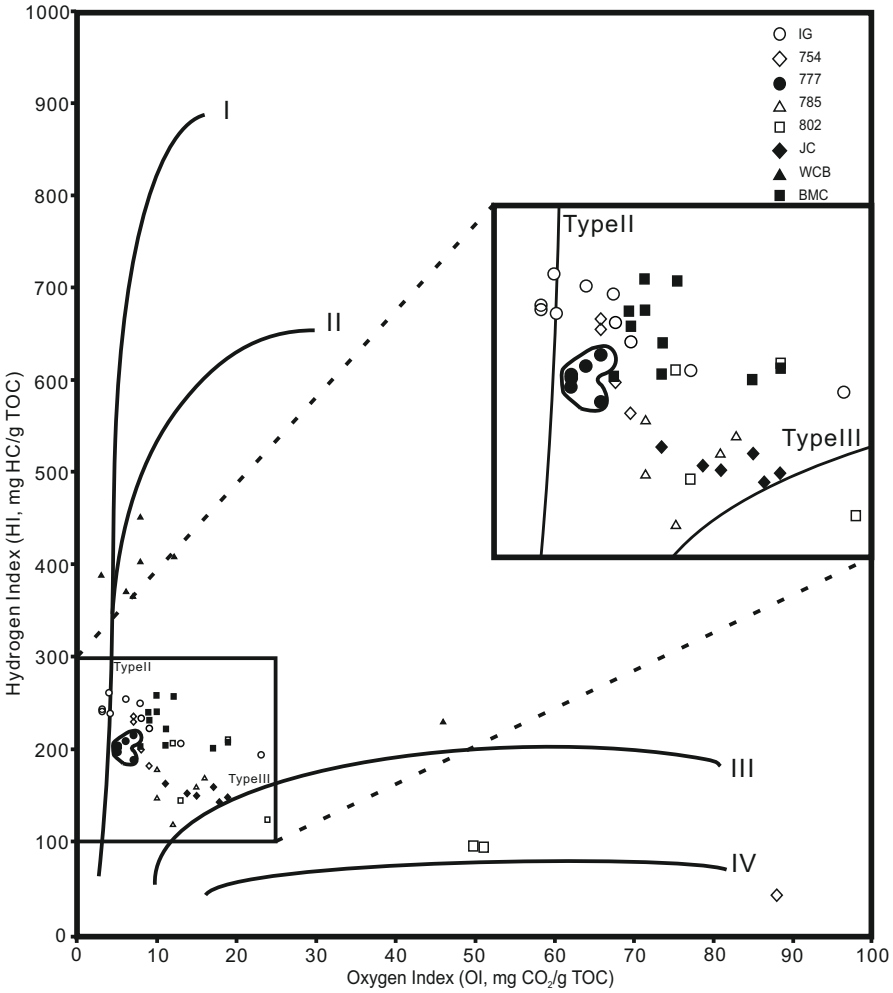
IG
754
777
785
802
JC
WCB
BMC
I
II
III
IV
TypeII
TypeIII
TypeII
TypeIII
Hydrogen Index (HI, mg HC/g TOC)
Oxygen Index (OI, mg CO2/g TOC)
0
100
200
300
400
500
600
700
800
900
1000
0
10
20
30
40
50
60
70
80
90
100

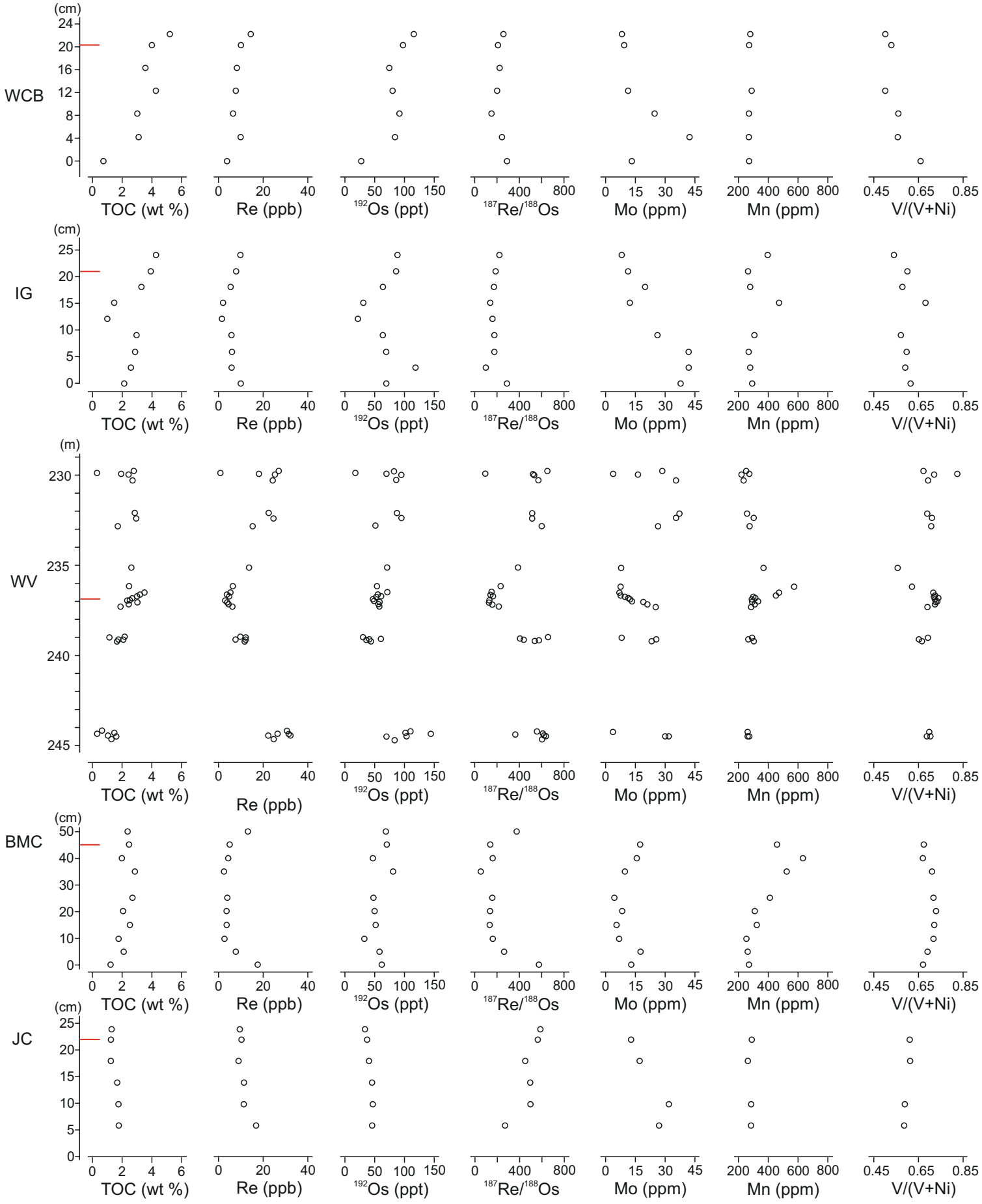
WCB
IG
WV
BMC
JC
(cm)
(m)
TOC (wt %)
Re (ppb)
192Os (ppt)
187Re/188Os
Mo (ppm)
Mn (ppm)
V/(V+Ni)

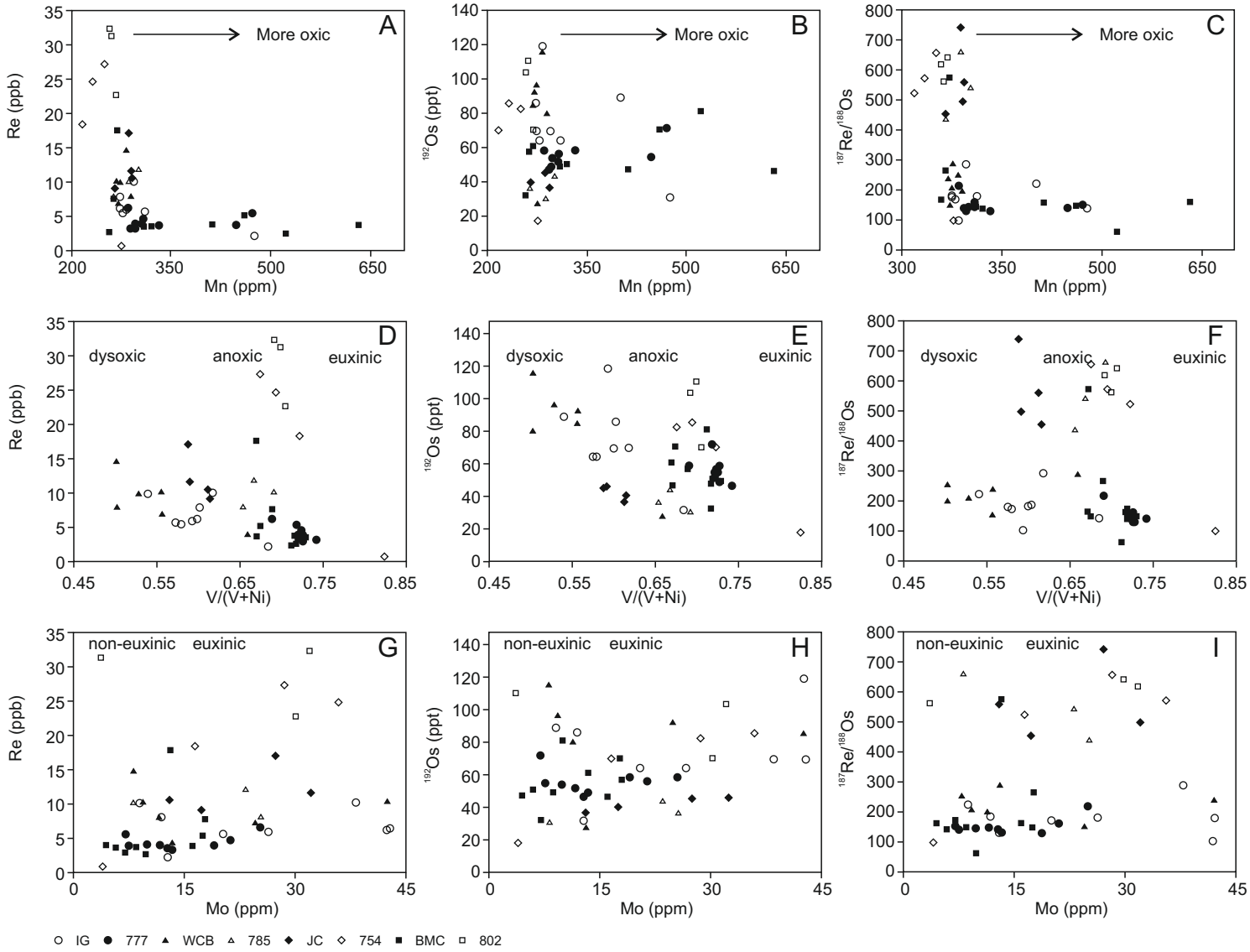
A
More oxic
Re (ppb)
Mn (ppm)
B
More oxic
^{192}Os (ppt)
Mn (ppm)
C
More oxic
^{187}Re/^{188}Os
Mn (ppm)
D
dysoxic
anoxic
euxinic
Re (ppb)
V/(V+Ni)
E
dysoxic
anoxic
euxinic
^{192}Os (ppt)
V/(V+Ni)
F
dysoxic
anoxic
euxinic
^{187}Re/^{188}Os
V/(V+Ni)
G
non-euxinic
euxinic
Re (ppb)
Mo (ppm)
H
non-euxinic
euxinic
^{192}Os (ppt)
Mo (ppm)
I
non-euxinic
euxinic
^{187}Re/^{188}Os
Mo (ppm)
IG
777
WCB
785
JC
754
BMC
802

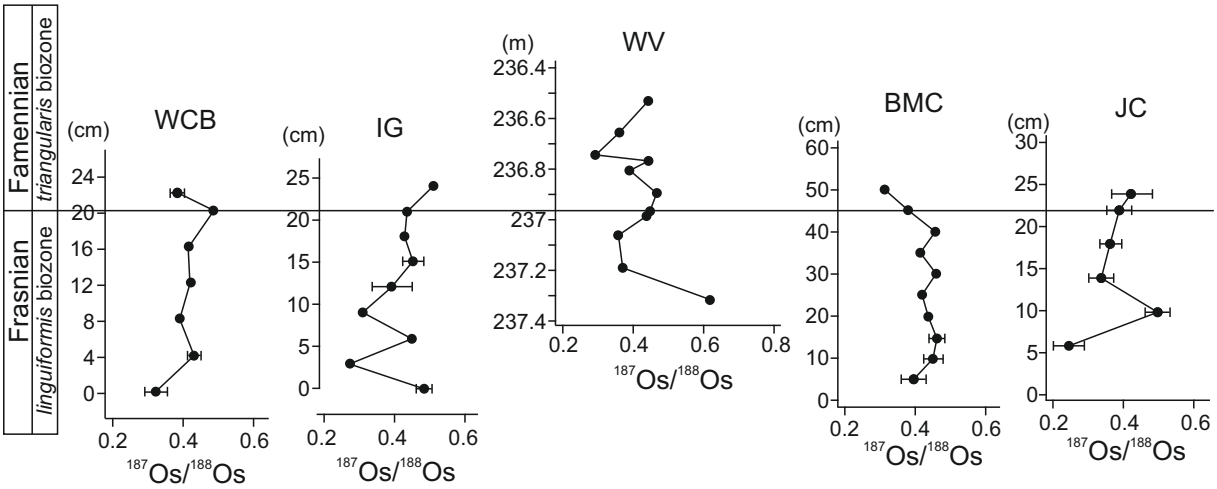
Famennian
triangularis biozone
Frasnian
linguiformis biozone
WCB
(cm)
24
20
16
12
8
4
0
0.2
0.4
0.6
187Os/188Os
IG
(cm)
25
20
15
10
5
0
0.2
0.4
0.6
187Os/188Os
WV
(m)
236.4
236.6
236.8
237
237.2
237.4
0.2
0.4
0.6
0.8
187Os/188Os
BMC
(cm)
60
50
40
30
20
10
0
0.2
0.4
0.6
187Os/188Os
JC
(cm)
30
25
20
15
10
5
0
0.2
0.4
0.6
187Os/188Os

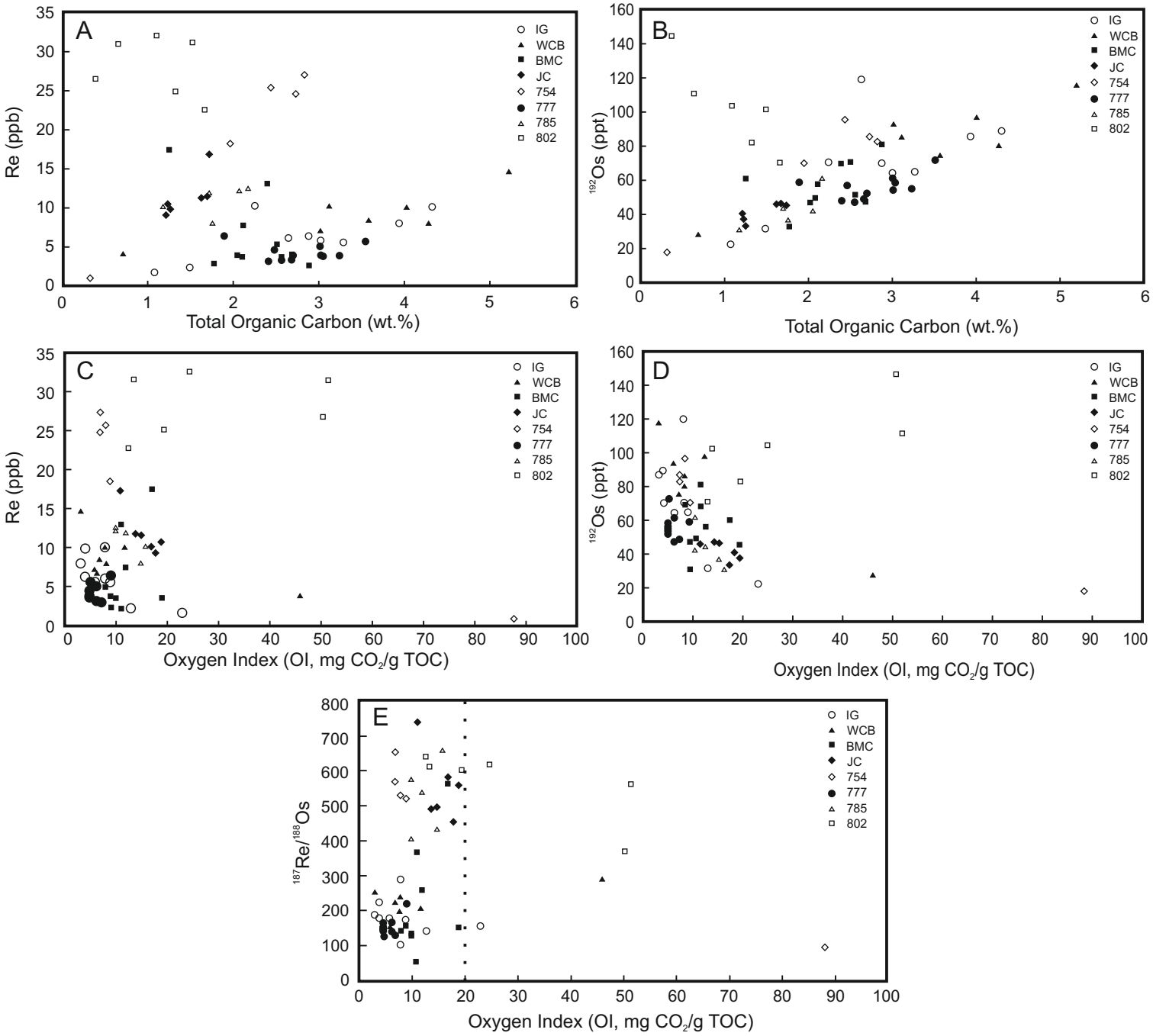
A
Re (ppb)
Total Organic Carbon (wt.%)
B
^{192}Os (ppt)
Total Organic Carbon (wt.%)
C
Re (ppb)
Oxygen Index (OI, mg CO$_2$/g TOC)
D
^{192}Os (ppt)
Oxygen Index (OI, mg CO$_2$/g TOC)
E
^{187}Re/^{188}Os
Oxygen Index (OI, mg CO$_2$/g TOC)
IG
WCB
BMC
JC
754
777
785
802

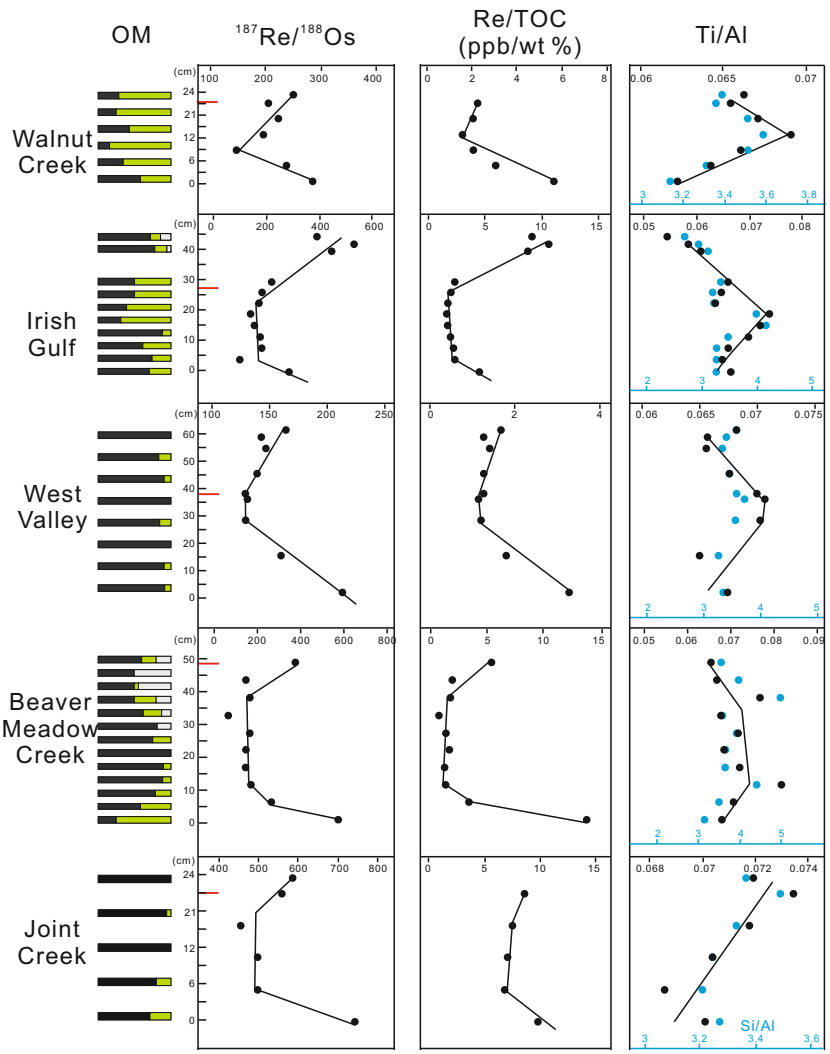
OM
$^{187}Re/^{188}Os$
Re/TOC (ppb/wt %)
Ti/Al
Walnut Creek
Irish Gulf
West Valley
Beaver Meadow Creek
Joint Creek
(cm)
Si/Al

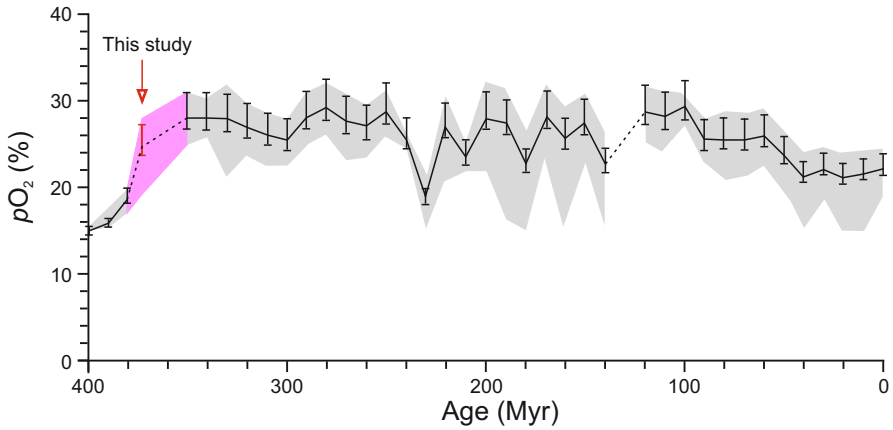
This study
pO_2 (%)
40
30
20
10
0
400
300
200
100
0
Age (Myr)

Table S1. Organic petrology data.

Sample ID	Depth (cm)	Mineral	Solid Bitumen	Tasmanites	Inertinites
B1-03	70	486	11	2	1
B1-02	65	487	11	1	1
B1-01	60	488	10	1	1
BMC_1_02	50	490	6	2	2
BMC_5	45	478	11	0	11
BMC_10	40	482	9	1	8
BMC_15	35	490	5	3	2
BMC_20	30	492	5	2	1
BMC_21	29	484	13	0	3
BMC_22	28	492	6	2	0
BMC_23	27	493	6	1	0
BMC_24	26	490	10	0	0
BMC_25	25	492	8	0	0
BMC_30	20	490	9	1	0
BMC_35	15	491	8	1	0
BMC_40	10	486	11	3	0
BMC_45	5	488	7	5	0
BMC_51	0	496	1	3	0
754	22982	490	5	4	1
754_4	22992	498	1	1	0
754_6	22997	486	8	5	1
754_8	23002	485	13	0	2
755_8	23033	486	11	2	1
761_6	23214	475	20	3	2
762_6	23241	482	8	7	3
764	23287	490	6	3	1
771_6	23515	493	5	0	2
774_10.5	23618	494	6	0	0
776	23652	464	35	0	1
776_9.5	23677	487	13	0	0
776_11	23680	488	10	2	0
777_2.5	23689	489	10	1	0
777_5.3	23696	487	13	0	0
777_6	23698	487	11	2	0
777_9	23706	270	8	0	0
778_2	23719	479	19	2	0
778_7	23731	488	11	1	0
784_1.5	23900	458	0	42	0
784_5.5	23910	483	17	0	0
784_6.5	23913	403	2	1	0
784_8	23917	495	0	5	0
784_10	23922	491	9	0	0
801_3	24422	488	0	12	0
801_7	24432	336	5	11	0

801_9	24437	422	5	2	0
802	24445	425	2	16	0
802_1.5	24449	487	1	12	0
802_9	24468	493	2	5	0
ZL-16-01	313	478	13	8	1
ZL-15-03	308	478	15	6	1
ZL_15_01	300	472	14	12	2
ZL_13_01	250	468	15	15	2
ZL_12-01	245	464	26	7	3
ZL_06_06	110.25	469	18	12	1
ZL_06_04	107.75	456	24	18	2
ZL_06_03	106.5	453	35	12	0
ZL_06_02	105.25	463	14	18	5
ZL-01-03	45	486	10	2	2
ZL-01-02	43	485	14	3	1
ZLV_01	24	485	14	3	1
ZLV_02	21	314	4	4	0
ZLV_04	15	314	4	4	0
ZLV_07	6	472	11	17	0
ZLV_09	0	484	5	11	0
WCB_B3_02	96	474	8	15	3
WCB_B3_04	92	472	7	15	6
WCB_B3_06	88	474	4	20	2
WCB_B3_08	84	466	15	18	1
WCB_B2_01	66	469	11	19	1
WCB_B2_07	62	459	10	27	4
WCB_B2_09	59	472	9	17	2
WCB_B1_02	28	461	23	13	3
WCB_FF_02	20	460	11	29	0
WCB_FF_04	16	470	7	23	0
WCB_FF_06	12	461	8	31	0
WCB_FF_08	8	479	7	14	0
WCB_FF_10	4	471	4	25	0
WCB_FF_12	0	468	14	18	0
JPC_D8	360	494	3	3	0
JPC_D6	355	492	4	4	0
JPC_D3	350	489	8	3	0
JPC_D1	345	494	4	2	0
JPC_FF_02	22	493	5	2	0
JPC_FF_04	18	495	4	1	0
JPC_FF_06	14	489	11	0	0
JPC_FF_08	10	482	17	1	0
JPC_FF_10	6	493	7	0	0

Inertinite abundance data is calculated as volume percent on a whole rock bas

Inertinite abundance-whole rock (%)
0.2
0.2
0.2
0.4
2.2
1.6
0.4
0.2
0.6
0
0
0
0
0
0
0
0
0
0.2
0
0.2
0.4
0.2
0.4
0.6
0.2
0.4
0
0.2
0
0
0
0
0
0
0
0
0
0
0
0
0
0
0

0
0
0
0
0.2
0.2
0.4
0.4
0.6
0.2
0.4
0
1
0.4
0.2
0.2
0
0
0
0
0.6
1.2
0.4
0.2
0.2
0.8
0.4
0.6
0
0
0
0
0
0
0
0
0
0
0
0
0
0
0
0
0

sis.

Table S2. Inertinite abundance data calculated as volume per

Sample ID	Mineral	Solid Bitumen	Tasmanites	Inertinite
B1-03	486	11	2	1
B1-02	487	11	1	1
B1-01	488	10	1	1
BMC_1_02	490	6	2	2
BMC_5	478	11	0	11
BMC_10	482	9	1	8
BMC_15	490	5	3	2
BMC_20	492	5	2	1
BMC_21	484	13	0	3
754	490	5	4	1
754_6	486	8	5	1
754_8	485	13	0	2
755_8	486	11	2	1
761_6	475	20	3	2
762_6	482	8	7	3
764	490	6	3	1
771_6	493	5	0	2
776	464	35	0	1
ZL-16-01	478	13	8	1
ZL-15-03	478	15	6	1
ZL_15_01	472	14	12	2
ZL_13_01	468	15	15	2
ZL_12-01	464	26	7	3
ZL_06_06	469	18	12	1
ZL_06_04	456	24	18	2
ZL_06_02	463	14	18	5
ZL-01-03	486	10	2	2
ZL-01-01	485	14	3	1
ZLV_01	485	14	3	1
WCB_B3_02	474	8	15	3
WCB_B3_04	472	7	15	6
WCB_B3_06	474	4	20	2
WCB_B3_08	465	15	18	1
WCB_B2_01	469	11	19	1
WCB_B2_07	459	10	27	4
WCB_B2_09	472	9	17	2
WCB_B1_02	461	23	13	3
average				
s.d.				

	value used for pO_2 % calculation	pO_2 %	formular
average	11.90	24.8	(1)
average	11.90	27.1	(2)

average	11.90	23.8	(3)
average-s.d.	1.52	19.4	(4)
average+s.d.	22.34	28.0	(5)

·cent on mineral-free basis.

Inertinite abundance-mineral free (%)
7.1
7.7
8.3
20.0
50.0
44.4
20.0
12.5
18.8
10.0
7.1
13.3
7.1
8.0
16.7
10.0
28.6
2.8
4.5
4.5
7.1
6.3
8.3
3.2
4.5
13.5
14.3
5.6
5.6
11.5
21.4
7.7
2.9
3.2
9.8
7.1
7.7
11.9
10.4

shaded area
shaded area

Table S3. Inertinite reflectance data.

Sample ID	Inertinite reflectance (%)	No. of measurements	s.d.
B1-03	1.98	101	0.93
B1-02	1.94	32	0.63
B1-01	1.74	100	0.93
BMC_1_02	1.91	100	0.63
BMC_5	3.17	100	1.35
BMC_10	2.64	100	1.1
BMC_15	2.05	100	1.04
BMC_20	1.86	100	0.99
BMC_21	2.08	100	1.27
754_6	2.85	104	0.9
754_8	2.78	100	0.78
755_8	2.25	100	0.71
761_6	2.89	100	1
762_6	3.16	100	1.11
764	2.83	100	1.27
771_6	2.26	100	0.86
ZL-16-01	2.07	101	0.88
ZL-15-03	2.14	100	0.68
ZL_15_01	2.36	100	0.71
ZL_13_01	2.93	100	1.06
ZL_12-01	2.31	100	0.85
ZL_06_02	2.95	100	0.87
WCB_B3_02	2.69	100	1.09
WCB_B3_04	2.72	100	0.82
WCB_B3_06	2.19	100	1.09
WCB_B3_08	2.55	100	0.88
WCB_B2_01	2.54	100	1.09
WCB_B2_07	2.11	100	0.92
WCB_B2_09	2.90	100	1.27
WCB_B1_02	2.42	100	0.77

Table S4. Re–Os abundance and isotope data.

Sample ID	Re (ppb)	±	Os (ppt)	±	^{192}Os (ppt)	±	^{187}Re/^{188}Os	±
WCB-FF-01	14.57	0.04	345.93	1.94	115.36	0.57	251.34	1.38
WCB-FF-02	9.95	0.06	283.33	1.41	96.36	0.41	205.36	1.55
WCB_FF_04	8.32	0.02	219.24	1.11	74.25	0.31	222.83	1.10
WCB_FF_06	7.90	0.03	232.14	1.16	80.00	0.35	196.40	1.08
WCB_FF_08	6.95	0.02	258.94	1.22	92.47	0.42	149.51	0.80
WCB_FF_10	10.10	0.03	253.18	1.32	84.84	0.37	236.75	1.19
WCB-FF-12	3.97	0.02	84.01	0.55	27.56	0.17	286.58	2.11
BMC_1_02	13.16	0.03	223.71	1.22	69.43	0.27	377.08	1.75
BMC_5	5.23	0.01	197.32	1.10	70.70	0.43	147.05	0.97
BMC_10	3.82	0.01	133.33	0.77	46.87	0.29	162.09	1.09
BMC_15	2.55	0.01	214.31	1.02	81.30	0.49	62.40	0.41
BMC_25	3.88	0.01	136.11	0.79	47.85	0.29	161.30	1.07
BMC_30	3.64	0.01	139.15	0.81	49.68	0.32	145.86	1.02
BMC_35	3.59	0.01	142.35	0.80	50.92	0.31	140.36	0.93
BMC_40	2.77	0.01	93.25	0.55	32.61	0.20	169.07	1.13
BMC_45	7.69	0.02	175.21	1.13	57.51	0.35	265.88	1.75
BMC_51	17.59	0.04	221.66	1.33	61.01	0.23	573.67	2.58
JPC_FF_01	9.98	0.02	124.39	0.99	33.92	0.21	585.35	3.93
JPC_FF_02	10.59	0.03	135.55	0.87	37.59	0.16	560.15	2.82
JPC_FF_04	9.25	0.02	137.11	0.84	40.42	0.17	455.17	2.28
JPC_FF_06	11.53	0.03	159.81	0.99	46.09	0.20	497.82	2.49
JPC_FF_08	11.72	0.03	165.02	1.01	46.94	0.19	496.54	2.51
JPC_FF_10	17.16	0.04	180.39	1.15	46.08	0.18	740.68	3.41
776.00	5.47	0.01	202.30	1.05	71.76	0.37	151.52	0.87
776_5	3.86	0.01	152.03	1.04	54.87	0.48	139.99	1.27
776_8.5	5.09	0.01	171.26	1.09	61.20	0.46	165.38	1.31
776_9.5	3.92	0.01	152.08	0.90	54.25	0.36	143.63	1.02
776_11	3.86	0.01	145.36	0.86	52.03	0.35	147.53	1.06
777_2.5	3.30	0.01	131.82	0.92	47.04	0.41	139.39	1.27
777_5.3	3.10	0.01	132.57	0.91	47.76	0.42	129.09	1.18
777_6	3.23	0.01	136.38	0.93	49.10	0.43	131.07	1.19
777_9	3.81	0.01	160.69	1.08	58.45	0.51	129.67	1.17
778_2	4.55	0.01	158.88	0.95	56.48	0.38	160.24	1.14
778_7	6.32	0.02	175.69	0.97	58.57	0.28	214.64	1.15
ZLV_01	9.96	0.02	265.64	1.36	89.10	0.38	222.43	1.09
ZLV_02	7.95	0.02	247.83	1.25	86.00	0.40	183.92	0.96
ZLV_03	5.56	0.01	184.27	1.02	64.53	0.36	171.53	1.05
ZLV_04	2.25	0.01	89.05	0.71	31.76	0.34	141.22	1.56
ZLV_05	1.71	0.00	61.33	0.76	21.80	0.44	156.10	3.21
ZLV_06	5.79	0.01	182.11	1.04	64.31	0.39	179.15	1.17
ZLV_07	6.30	0.02	200.60	1.07	69.65	0.35	179.95	1.02
ZLV_08	6.04	0.01	317.75	1.50	119.12	0.67	100.95	0.62
ZLV_09	10.11	0.02	216.87	1.18	69.95	0.30	287.53	1.41
754.00	27.16	0.07	312.74	1.95	82.56	0.32	654.41	2.96
754_4	0.87	0.00	48.54	0.71	17.84	0.48	97.46	2.66

754_6	18.37	0.04	250.37	1.60	70.12	0.31	521.07	2.61
754_8	25.52	0.06	345.66	2.34	95.38	0.45	532.30	2.81
755_8	24.61	0.06	309.52	1.88	85.82	0.34	570.55	2.64
761_6	22.63	0.06	307.89	1.76	87.43	0.31	514.99	2.23
762_6	24.74	0.06	332.76	1.89	95.26	0.34	516.64	2.24
764.00	15.61	0.04	190.26	1.19	51.37	0.20	604.46	2.81
771_6	13.84	0.03	233.03	1.32	71.07	0.28	387.27	1.81
774_10.5	6.43	0.02	164.82	0.96	54.85	0.29	233.27	1.34
784_1.5	10.08	0.02	115.92	1.52	30.49	0.42	658.01	9.24
784_5.5	12.49	0.03	199.73	1.96	60.94	0.64	407.86	4.43
784_6.5	7.97	0.02	126.69	1.55	36.40	0.50	435.69	6.12
784_8	12.11	0.03	152.31	1.65	41.75	0.44	577.17	6.28
784_10	11.83	0.03	156.47	1.67	43.56	0.46	540.43	5.88
801_3	31.14	0.08	394.47	3.74	110.60	0.96	560.20	5.06
801_7	31.37	0.08	375.73	3.65	101.90	0.89	612.41	5.53
801_9	26.64	0.06	459.79	3.89	144.51	1.26	366.72	3.32
802.00	32.21	0.08	384.99	2.29	103.89	0.37	616.85	2.70
802_1.5	22.63	0.09	262.63	1.59	70.34	0.26	640.07	3.41
802_9	24.90	0.06	303.64	3.31	82.55	0.87	600.19	6.52
ZL-01-04	10.56	0.03	175.16	1.13	53.05	0.27	396.21	2.24
ZL-01-03	25.81	0.06	340.74	1.96	95.24	0.34	539.13	2.32
ZL-01-02	22.38	0.05	336.27	1.84	99.29	0.35	448.42	1.94

[a]Only the samples close to the F-F interval were calculated for Os_i.
Initial Os isotope composition (Osi) is calculated at 371.93 Ma (Percival et al., 2018). All unce
the associated error correlation (Ludwig, 1980).

$^{187}Os/^{188}Os$	±	rho	Os_i [a]	±
1.95	###	0.63	0.39	0.02
1.77	###	0.39	0.49	0.02
1.81	###	0.60	0.42	0.02
1.64	###	0.57	0.42	0.02
1.32	###	0.59	0.39	0.01
1.91	###	0.61	0.43	0.02
2.11	###	0.60	0.33	0.03
2.66	###	0.60	0.31	0.03
1.29	###	0.65	0.38	0.02
1.46	###	0.65	0.46	0.02
0.80	###	0.65	0.42	0.01
1.46	###	0.65	0.46	0.02
1.33	###	0.65	0.42	0.02
1.31	###	0.65	0.44	0.02
1.51	###	0.66	0.46	0.02
2.10	###	0.65	0.45	0.03
3.96	###	0.59	0.39	0.04
4.07	###	0.66	0.43	0.06
3.87	###	0.62	0.39	0.04
3.20	###	0.61	0.37	0.03
3.43	###	0.61	0.34	0.04
3.59	###	0.58	0.50	0.04
4.85	###	0.59	0.25	0.05
1.38	###	0.64	0.44	0.02
1.23	###	0.68	0.36	0.02
1.32	###	0.67	0.29	0.02
1.33	###	0.66	0.44	0.02
1.30	###	0.66	0.39	0.02
1.33	###	0.68	0.46	0.02
1.25	###	0.68	0.44	0.02
1.25	###	0.68	0.44	0.02
1.16	###	0.68	0.36	0.02
1.36	###	0.66	0.37	0.02
1.95	###	0.63	0.62	0.02
1.90	###	0.61	0.51	0.02
1.58	###	0.62	0.44	0.02
1.50	###	0.65	0.43	0.02
1.34	###	0.69	0.46	0.03
1.37	###	0.70	0.40	0.06
1.42	###	0.66	0.31	0.02
1.58	###	0.64	0.46	0.02
0.90	###	0.65	0.28	0.01
2.27	###	0.61	0.49	0.02
4.45	###	0.60		
1.07	###	0.70		

3.76	###	0.62
3.93	###	0.63
3.88	###	0.61
3.61	###	0.58
3.52	###	0.58
4.18	###	0.60
2.84	###	0.60
1.97	###	0.64
4.50	###	0.70
2.83	###	0.69
3.48	###	0.70
4.01	###	0.69
3.83	###	0.69
3.75	###	0.68
4.13	###	0.68
2.53	###	0.68
4.19	###	0.58
4.28	###	0.48
4.10	###	0.69
2.91	###	0.64
3.78	###	0.58
3.18	###	0.58

ertainties are at 2σ level. Rho (ρ) is

Table S5. Major element data.

Sample ID	Al2O3 %	SiO2 %	TiO2 %	Si %	Ti %	Al %	Si/Al
WCB B3-02	13.665	66.263	0.857	30.973	0.514	7.232	4.283
WCB B3-08	15.386	60.254	0.868	28.164	0.520	8.143	3.459
WCB 02-01	12.813	58.414	0.775	27.304	0.464	6.781	4.026
WCB B2-09	14.535	63.342	0.865	29.607	0.518	7.693	3.849
WCB 01-02	17.226	55.885	0.858	26.122	0.514	9.117	2.865
WCB-FF-01	15.288	58.642	0.893	27.366	0.535	8.087	3.384
WCB-FF-02	15.647	59.476	0.904	27.755	0.542	8.277	3.353
WCB_FF_04	15.402	61.266	0.912	28.591	0.547	8.148	3.509
WCB_FF_06	14.948	60.678	0.912	28.316	0.547	7.907	3.581
WCB_FF_08	15.550	61.949	0.907	28.910	0.544	8.226	3.514
WCB_FF_10	16.064	60.241	0.911	28.112	0.546	8.498	3.308
WCB-FF-12	17.036	60.367	0.937	28.171	0.562	9.012	3.126
BMC B1-03	15.46	62.857	0.919	29.381	0.551	8.182	3.591
BMC B1-02	15.223	63.683	0.928	29.767	0.556	8.057	3.695
BMC B1-01	15.636	62.791	0.916	29.350	0.549	8.275	3.547
BMC_1_02	14.722	59.209	0.853	27.631	0.511	7.788	3.548
BMC_5	13.807	61.615	0.820	28.754	0.491	7.304	3.937
BMC_10	11.374	64.052	0.774	29.891	0.464	6.017	4.968
BMC_15	14.406	58.430	0.864	27.267	0.518	7.621	3.578
BMC_25	14.297	63.597	0.908	29.679	0.544	7.563	3.924
BMC_30	15.275	63.269	0.928	29.526	0.556	8.080	3.654
BMC_35	15.205	63.029	0.969	29.414	0.581	8.043	3.657
BMC_40	13.603	68.075	0.987	31.768	0.592	7.196	4.415
BMC_45	15.804	62.663	0.992	29.243	0.595	8.360	3.498
BMC_51	16.888	60.082	1.017	28.038	0.610	8.934	3.138
JPC D8	18.129	60.901	1.009	28.466	0.605	9.595	2.967
JPC D6	18.621	59.361	0.972	27.747	0.583	9.855	2.815
JPC D3	17.849	59.961	0.956	28.027	0.573	9.447	2.967
JPC D-01	16.493	63.474	0.968	29.669	0.580	8.729	3.399
JPC_FF_01	16.343	62.322	1.038	29.084	0.622	8.645	3.364
JPC_FF_02	16.091	63.684	1.044	29.719	0.626	8.512	3.491
JPC_FF_04	16.701	63.095	1.057	29.444	0.633	8.835	3.333
JPC_FF_06	16.721	61.486	1.039	28.693	0.623	8.845	3.244
JPC_FF_08	16.950	61.687	1.026	28.787	0.615	8.967	3.211
JPC_FF_10	16.702	61.891	1.034	28.882	0.620	8.835	3.269
754	14.224	63.922	0.868	29.830	0.520	7.524	3.964
754_4	20.019	56.993	0.902	26.597	0.541	10.59	2.511
754_6	13.395	67.403	0.858	31.455	0.514	7.086	4.439
754_8	13.561	66.814	0.892	31.180	0.535	7.174	4.346
755_8	12.933	67.171	0.830	31.346	0.497	6.842	4.582
761_6	16.014	60.869	0.899	28.451	0.539	8.475	3.357
762_6	13.650	65.291	0.896	30.469	0.537	7.221	4.220
764	14.851	64.465	0.872	30.084	0.523	7.856	3.829
771_6	15.569	60.942	0.889	28.440	0.533	8.236	3.453
774_10.5	12.260	62.273	0.787	29.061	0.472	6.486	4.481
776	14.198	60.448	0.838	28.209	0.502	7.511	3.756

776_5	13.546	62.930	0.878	29.367	0.526	7.166	4.098
776_8.5	15.141	61.560	0.911	28.728	0.546	8.010	3.587
776_9.5	15.857	61.000	0.919	28.467	0.551	8.388	3.394
776_11	15.957	60.388	0.922	28.181	0.553	8.441	3.338
777_2.5	15.790	61.854	0.942	28.865	0.565	8.353	3.456
777_5.3	15.417	62.735	0.953	29.276	0.571	8.156	3.590
777_6	15.010	63.465	0.936	29.617	0.561	7.940	3.730
777_9	15.356	62.361	0.953	29.102	0.571	8.123	3.582
778_2	16.399	60.846	0.941	28.395	0.564	8.675	3.273
778_7	16.333	61.842	0.973	28.860	0.583	8.640	3.340
784_1.5	15.727	63.323	0.996	29.551	0.597	8.320	3.552
784_5.5	15.126	64.451	0.995	30.077	0.596	8.002	3.759
784_6.5	15.005	64.091	0.978	29.909	0.586	7.938	3.768
784_8	15.515	63.768	0.993	29.758	0.595	8.207	3.626
784_10	15.381	61.653	0.975	28.771	0.584	8.137	3.536
801_3	16.819	62.897	0.962	29.352	0.577	8.897	3.299
801_7	16.896	61.223	0.984	28.571	0.590	8.938	3.197
801_9	20.082	58.137	0.993	27.131	0.595	10.62	2.554
802	15.905	63.100	1.013	29.447	0.607	8.414	3.500
802_1.5	17.334	59.010	0.987	27.538	0.592	9.170	3.003
802_9	14.994	65.491	1.009	30.562	0.605	7.932	3.853
ZL-16-01	14.387	64.657	0.87	30.222	0.521	7.614	3.969
ZL-15-01	13.853	65.129	0.873	30.443	0.523	7.332	4.152
ZL-13-01	15.733	60.513	0.909	28.285	0.545	8.327	3.397
ZL-12-01	15.806	61.458	0.933	28.727	0.559	8.365	3.434
ZL-06-06	17.424	58.98	0.902	27.568	0.541	9.222	2.990
ZL-06-02	16.379	60.152	0.9	28.116	0.539	8.669	3.243
ZL-01-04	18.608	57.094	0.893	26.644	0.535	9.844	2.707
ZL-01-03	17.042	56.753	0.878	26.485	0.526	9.015	2.938
ZL-01-02	16.271	57.101	0.869	26.647	0.521	8.607	3.096
ZLV_01	15.061	57.064	0.876	26.630	0.525	7.967	3.342
ZLV_02	16.427	59.199	0.937	27.626	0.562	8.690	3.179
ZLV_03	15.849	58.010	0.888	27.071	0.532	8.384	3.229
ZLV_04	14.429	65.154	0.942	30.405	0.565	7.633	3.983
ZLV_05	14.275	67.898	0.908	31.686	0.544	7.551	4.196
ZLV_06	15.625	61.166	0.963	28.544	0.577	8.266	3.453
ZLV_07	16.414	60.910	0.954	28.425	0.572	8.683	3.274
ZLV_08	16.272	60.374	0.934	28.175	0.560	8.608	3.273
ZLV_09	16.590	61.240	0.973	28.579	0.583	8.776	3.256

Ti/Al
0.071
0.064
0.068
0.067
0.056
0.066
0.065
0.067
0.069
0.066
0.064
0.062
0.067
0.069
0.066
0.066
0.067
0.077
0.068
0.072
0.069
0.072
0.082
0.071
0.068
0.063
0.059
0.061
0.066
0.072
0.074
0.072
0.070
0.069
0.070
0.069
0.051
0.073
0.075
0.073
0.064
0.074
0.067
0.065
0.073
0.067

0.073
0.068
0.066
0.065
0.068
0.070
0.071
0.070
0.065
0.067
0.072
0.075
0.074
0.073
0.072
0.065
0.066
0.056
0.072
0.065
0.076
0.068
0.071
0.065
0.067
0.059
0.062
0.054
0.058
0.061
0.066
0.065
0.063
0.074
0.072
0.070
0.066
0.065
0.066

Table S6. Trace element data.

Sample ID	Mn (ppm)	V (ppm)	Ni (ppm)	Mo (ppm)	V/(V+Ni)
WCB-FF-01	283.24	127.71	126.42	8.04	0.50
WCB-FF-02	274.07	129.10	115.21	9.29	0.53
WCB_FF_06	289.53	118.66	117.48	11.37	0.50
WCB_FF_08	271.11	118.75	94.44	24.71	0.56
WCB_FF_10	269.39	120.04	95.65	42.35	0.56
WCB-FF-12	275.15	123.76	64.22	13.14	0.66
BMC_5	459.79	102.73	49.45	17.64	0.68
BMC_10	631.36	84.08	41.26	16.10	0.67
BMC_15	521.85	108.31	43.77	9.97	0.71
BMC_25	412.34	105.32	41.56	4.57	0.72
BMC_30	309.54	113.88	42.34	8.63	0.73
BMC_35	320.66	113.92	44.37	5.90	0.72
BMC_40	258.11	97.71	38.38	7.06	0.72
BMC_45	264.45	114.67	51.58	17.87	0.69
BMC_51	270.16	127.12	62.54	13.31	0.67
JPC_FF_02	292.84	115.94	73.46	13.10	0.61
JPC_FF_04	265.60	118.95	74.48	17.39	0.61
JPC_FF_08	290.42	125.78	87.17	32.17	0.59
JPC_FF_10	287.41	120.80	84.63	27.24	0.59
754.00	250.18	113.23	54.46	28.46	0.68
754_4	276.03	155.46	33.13	3.92	0.82
754_6	217.43	106.15	40.87	16.50	0.72
755_8	232.99	103.95	45.78	35.73	0.69
761_6	255.77	125.68	56.19	37.10	0.69
762_6	300.25	110.12	44.72	35.32	0.71
764.00	273.83	109.29	44.88	26.48	0.71
771_6	365.14	121.69	95.92	7.71	0.56
774_10.5	570.69	97.16	58.38	7.63	0.62
776.00	471.01	106.60	41.80	7.04	0.72
776_5	448.03	101.10	38.94	7.53	0.72
776_9.5	297.88	119.38	45.57	9.88	0.72
776_11	306.92	119.86	46.48	11.70	0.72
777_2.5	291.69	119.83	41.64	12.74	0.74
777_6	295.87	114.17	43.01	13.34	0.73
777_9	331.82	116.19	43.72	18.97	0.73
778_2	307.47	124.62	47.58	21.20	0.72
778_7	284.70	122.68	55.17	25.25	0.69
784_1.5	287.28	116.86	52.09	8.23	0.69
784_6.5	264.41	110.66	58.46	25.41	0.65
784_10	301.80	119.39	59.37	23.29	0.67
801_3	261.53	126.52	54.35	3.67	0.70
802.00	258.11	131.52	58.56	31.91	0.69
802_1.5	267.71	142.64	59.54	30.02	0.71
ZL-01-04	376.23	140.02	50.83	4.75	0.73
ZL-01-03	398.43	134.24	88.19	18.61	0.60
ZL-01-02	374.25	132.02	90.40	20.54	0.59

ZLV_01	399.97	117.50	100.41	8.77	0.54
ZLV_02	272.18	127.99	84.97	11.74	0.60
ZLV_03	277.22	122.85	89.63	20.04	0.58
ZLV_04	474.36	106.55	49.41	12.47	0.68
ZLV_06	309.82	117.03	87.30	26.29	0.57
ZLV_07	272.58	123.11	82.80	42.39	0.60
ZLV_08	282.15	121.04	83.50	42.08	0.59
ZLV_09	293.54	119.44	74.31	38.03	0.62

Table S7. Bitumen reflectance data.

Sample ID	BRo (%)	No. of measurements	s.d.
B1-03	0.56	50	0.073
B1-02	0.66	62	0.158
B1-01	0.53	51	0.084
BMC_1_02	0.66	50	0.158
BMC_5	0.64	50	0.167
BMC_10	0.73	50	0.083
BMC_15	0.56	50	0.076
BMC_20	0.60	51	0.098
BMC_21	0.56	70	0.016
BMC_22	0.65	50	0.115
BMC_25	0.55	50	0.080
BMC_30	0.56	100	0.112
BMC_35	0.54	50	0.106
BMC_40	0.60	53	0.118
BMC_45	0.59	50	0.106
BMC_51	0.57	33	0.076
754_6	0.60	25	0.163
755_8	0.62	27	0.146
761_6	0.61	81	0.086
762_6	0.61	25	0.146
771_6	0.66	25	0.141
776	0.58	25	0.078
776_9.5	0.68	30	0.118
776_11	0.60	26	0.104
777_2.5	0.64	26	0.099
777_5.3	0.58	25	0.070
777_6	0.56	26	0.066
777_9	0.56	26	0.096
778_7	0.60	25	0.125
784_1.5	0.63	25	0.106
784_5.5	0.66	30	0.072
784_8	0.61	26	0.113
801_7	0.64	28	0.160
801_9	0.63	23	0.180
802	0.63	20	0.140
802_9	0.53	14	0.139
ZL-16-01	0.73	25	0.220
ZL_06_04	0.70	25	0.165
ZL_06_02	0.62	25	0.167
ZL-01-03	0.67	50	0.104
ZL-01-02	0.65	50	0.090
ZLV_02	0.60	25	0.070
ZLV_04	0.63	25	0.127
WCB_B3_02	0.49	30	0.056
WCB_B3_04	0.46	50	0.058
WCB_B3_06	0.49	30	0.099

WCB_B3_08	0.62	50	0.091
WCB_B2_01	0.55	70	0.116
WCB_B2_07	0.48	50	0.092
WCB_B2_09	0.46	50	0.093
WCB_B1_02	0.57	30	0.090
WCB_FF_02	0.50	59	0.089
WCB_FF_06	0.59	30	0.096
WCB_FF_08	0.43	30	0.069
WCB_FF_10	0.50	30	0.107
WCB_FF_12	0.51	30	0.081
JPC_D8	0.67	50	0.142
JPC_D6	0.68	50	0.106
JPC_D3	0.57	30	0.137
JPC_D1	0.55	50	0.061
JPC_FF_02	0.69	50	0.087
JPC_FF_04	0.72	50	0.088
JPC_FF_06	0.69	52	0.109
JPC_FF_08	0.70	30	0.077
JPC_FF_10	0.67	50	0.082

Table S8. TOC and programmed pyrolysis data.

Sample ID	TOC	S1	S2	S3	Tmax (℃)	HI	OI
WCB-FF-01	5.23	2.09	20.21	0.16	442	388	3
WCB-FF-02	4.03	1.89	16.45	0.5	443	408	12
WCB_FF_04	3.59	1.75	13.19	0.24	443	367	7
WCB_FF_06	4.3	1.93	17.39	0.35	443	404	8
WCB_FF_08	3.03	1.44	11.23	0.19	443	371	6
WCB_FF_10	3.13	1.59	14.15	0.26	446	452	8
WCB-FF-12	0.69	1.03	1.57	0.32	442	228	46
BMC_1_02	2.4	1.28	4.94	0.27	440	206	11
BMC_5	2.51	1.25	5.11	0.21	442	204	8
BMC_10	2.05	1.11	4.28	0.39	442	209	19
BMC_15	2.89	1.5	6.45	0.33	442	223	11
BMC_25	2.69	1.73	6.28	0.24	444	233	9
BMC_30	2.09	1.44	5.03	0.21	442	241	10
BMC_35	2.57	1.8	6.65	0.25	442	259	10
BMC_40	1.78	1.16	4.29	0.16	441	241	9
BMC_45	2.13	1.36	5.48	0.26	442	257	12
BMC_51	1.27	0.73	2.55	0.22	443	201	17
JPC_FF_01	1.25	0.5	2.03	0.21	444	161	17
JPC_FF_02	1.23	0.52	1.84	0.23	443	150	19
JPC_FF_04	1.22	0.54	1.76	0.22	444	144	18
JPC_FF_06	1.63	0.64	2.48	0.24	442	152	15
JPC_FF_08	1.69	0.68	2.59	0.24	444	153	14
JPC_FF_10	1.74	0.68	2.85	0.2	444	164	11
754	2.83	1.25	6.66	0.19	446	235	7
754_4	0.32	0.08	0.13	0.28	437	41	88
754_6	1.96	0.9	3.57	0.17	444	182	9
754_8	2.44	1.18	4.87	0.19	446	200	8
755_8	2.74	1.22	6.34	0.18	444	231	7
761_6	2.86	1.33	6.71	0.25	443	235	9
762_6	3.01	1.3	7.32	0.17	446	243	6
764	1.72	0.83	3.25	0.2	445	189	12
771_6	2.65	0.99	4.35	0.22	445	164	8
774_10.5	2.48	0.97	4.22	0.24	444	170	10
776	3.53	1.58	7.16	0.19	447	203	5
776_5	3.25	1.68	7.52	0.17	445	231	5
776_8.5	3.02	1.61	6.53	0.17	442	216	6
776_9.5	3.03	1.47	5.99	0.15	444	198	5
776_11	2.71	1.43	5.50	0.14	445	203	5
777_2.5	2.57	1.37	5.38	0.15	444	209	6
777_5.3	2.41	1.30	4.52	0.18	443	188	7
777_6	2.68	1.41	5.77	0.18	445	215	7
777_9	3.05	1.65	6.17	0.15	444	202	5
778_2	2.48	1.34	5.54	0.12	444	223	5
778_7	1.9	1.27	3.77	0.17	445	198	9
784_1.5	1.18	0.55	1.98	0.19	446	168	16
784_5.5	2.17	1.15	3.85	0.21	445	177	10

784_6.5	1.76	0.85	2.8	0.27	442	159	15
784_8	2.06	0.87	3.02	0.21	443	147	10
784_10	1.71	0.75	2.02	0.2	445	118	12
801_3	0.65	0.22	0.61	0.33	442	94	51
801_7	1.51	0.62	2.17	0.2	443	144	13
801_9	0.38	0.14	0.36	0.19	439	95	50
802	1.1	0.41	1.35	0.26	443	123	24
802_1.5	1.67	0.74	3.46	0.2	445	207	12
802_9	1.33	0.61	2.79	0.25	445	210	19
ZL-01-04	1.16	0.49	1.8	0.18	445	155	16
ZL-01-03	2.44	1.16	4.91	0.15	444	201	6
ZL-01-02	2.54	1.22	5.17	0.12	445	204	5
ZLV_01	4.3	2.07	11.23	0.18	444	261	4
ZLV_02	3.92	1.62	9.51	0.13	448	243	3
ZLV_03	3.26	1.61	7.29	0.28	444	224	9
ZLV_04	1.46	0.89	3.01	0.19	444	206	13
ZLV_05	1.04	0.71	2.02	0.24	441	194	23
ZLV_06	2.99	1.68	7.64	0.18	446	256	6
ZLV_07	2.85	1.43	6.82	0.12	448	239	4
ZLV_08	2.62	1.37	6.57	0.2	446	251	8
ZLV_09	2.22	1.3	5.19	0.18	448	234	8

PI	S2/S3	S1/TOC*100
0.09	126	40
0.1	33	47
0.12	55	49
0.1	50	45
0.11	59	48
0.1	54	51
0.4	5	149
0.21	18	53
0.2	24	50
0.21	11	54
0.19	20	52
0.22	26	64
0.22	24	69
0.21	27	70
0.21	27	65
0.2	21	64
0.22	12	57
0.2	10	40
0.22	8	42
0.23	8	44
0.21	10	39
0.21	11	40
0.19	14	39
0.16	35	44
0.4	0.5	25
0.2	21	46
0.19	26	48
0.16	35	45
0.17	27	47
0.15	43	43
0.2	16	48
0.18	20	37
0.19	18	39
0.18	38	45
0.18	44	52
0.2	38	53
0.2	40	49
0.21	39	53
0.2	36	53
0.22	25	54
0.2	32	53
0.21	41	54
0.19	46	54
0.25	22	67
0.22	10	47
0.23	18	53

0.23	10	48
0.22	14	42
0.27	10	44
0.27	**2**	34
0.22	11	41
0.28	2	37
0.23	5	37
0.18	17	44
0.18	11	46
0.21	10	42
0.19	33	48
0.19	43	48
0.16	62	48
0.15	73	41
0.18	26	49
0.23	16	61
0.26	8	68
0.18	42	56
0.17	57	50
0.17	33	52
0.2	29	59